Additive Manufacturing 113 (2025) 105023

Contents lists available at ScienceDirect

Additive Manufacturing

journal homepage: www.elsevier.com/locate/addma

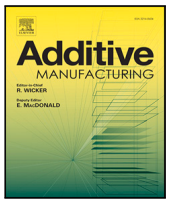

Research paper

An orientation-based homogenization approach for predicting process-induced deformations in extrusion-based additive manufacturing

Felix Frölich [a,*], Mario Emanuele Di Nardo [b], Constantin Krauß [a], Anselm Heuer [c], Wilfried V. Liebig [c], Florian Wittemann [a], Pierpaolo Carlone [b], Luise Kärger [a]

[a] Karlsruhe Institute of Technology (KIT), Institute of Vehicle System Technology - Lightweight Engineering, Rintheimer Querallee 2, Karlsruhe, 76131, Germany
[b] University of Salerno, Department of Industrial Engineering, 132 Via Giovanni Paolo II, Fisciano (SA), 84084, Italy
[c] Karlsruhe Institute of Technology (KIT), Institute for Applied Materials - Materials Science and Engineering, Engelbert-Arnold-Straße 4, Karlsruhe, 76131, Germany

ARTICLE INFO

Keywords:
Additive manufacturing (AM)
Fused filament fabrication
Material extrusion (MEX)
Fused deposition modeling
Finite element modeling
Homogenization
Warpage
PLA

ABSTRACT

This work presents a homogenization approach for considering process-specific mesostructures typical for material extrusion in finite element simulations to predict process-induced deformation. The approach is based on adapted orientation tensors and orientation averaging, accounting for the characteristic mesostructure and directionality of the material extrusion process. The method addresses the challenge of modeling mesostructural effects across entire components with computationally feasible element sizes. It is implemented in *Python* and *Abaqus*, and validated experimentally with PLA, showing good agreement between measured and predicted process-induced deformation. Comparative simulations with an isotropic stiffness formulation demonstrate the significant impact of considering mesostructural anisotropy, highlighting improvements over conventional approaches. Numerical studies further show the evolution of effective material orientation during printing, underscoring the advantages of the anisotropic approach. This method enables efficient, physically consistent integration of material extrusion mesostructures into process-induced deformation prediction, supporting enhanced process design and reliability in material extrusion manufactured components.

1. Introduction

1.1. Motivation and state of the art

Additive manufacturing (AM) enables the layer-by-layer production of components with a high degree of design freedom, overcoming the limitations of conventional tooling while reducing material waste and manufacturing costs, particularly in the production of complex or customized components and small series. This paper addresses the AM technology material extrusion (MEX), referred to as fused filament fabrication (FFF) when using filaments as feedstock, and known commercially as fused deposition modeling (FDM). This emerging process for unreinforced [1] and fiber-reinforced [2,3] thermoplastic components is of increasing industrial interest due to its ability to precisely orient materials locally [4] and introduce controlled anisotropy [5]. In particular, fiber-reinforced filaments enable load-adapted designs due to the high fiber orientation in the extrusion direction [6]. A major challenge in the production of such components is process-induced deformation (PiD) [7], which complicates the processability of warp-sensitive polymers [8,9]. The large number of possible printing parameters directly influence component quality [10] and makes experimental optimization time-consuming. This underscores the potential of numerical simulation to predict PiD, thereby improving processability and reducing costly trial-and-error approaches.

Finite element (FE) methods are the predominant approach for predicting PiD and residual stresses in MEX additive manufacturing [11–14]. The common macroscopic simulation strategy homogenizes the strand geometry and voids rather than explicitly modeling them. Zhang and Chou [11,12] pioneered FE simulations of MEX by progressively activating initially inactive elements along the G-Code-defined deposition path. This element activation method, also implemented in commercial software like *Abaqus* [15,16] or *Digimat-AM* [17], enables the temporal and spatial representation of extrusion-based deposition.

The simulation begins with component discretization into finite elements, which are activated stepwise according to the printing sequence. *Abaqus* supports partial element activation, allowing multiple strands or layers to be modeled within a single element by scaling the element mass proportional to the actual printed volume, thus improving the representation of material distribution. The process simulation

* Corresponding author.
E-mail address: felix.froelich@kit.edu (F. Frölich).

https://doi.org/10.1016/j.addma.2025.105023
Received 16 June 2025; Received in revised form 16 October 2025; Accepted 11 November 2025
Available online 12 November 2025
2214-8604/© 2025 The Authors. Published by Elsevier B.V. This is an open access article under the CC BY license (http://creativecommons.org/licenses/by/4.0/).

approaches typically use a sequentially coupled thermomechanical approach, where transient temperature fields from the thermal simulation serve as thermal loads in the subsequent mechanical simulation to compute stresses and deformation. The initial element temperature corresponds to the extrusion temperature. In *Abaqus*, the deposition strategy is controlled by an so called event series, which specifies the timing, path, and extrusion status [15].

Due to the small size of individual strands relative to the component, modeling every strand separately is computationally infeasible. Therefore, multiple filaments are combined into single elements. Because extrusion occurs along defined trajectories, local anisotropic material structures arise, leading to anisotropic stiffness within elements [18–20].

However, most simulations model the material as temperature-dependent but isotropic. For instance, Zhou et al. [21] use a thermoelastic isotropic polymer model, and Cattenone et al. [22] apply a thermo-elasto-plastic model without considering process-induced anisotropy. Abaqus-based studies (e.g., Brenken et al. [14,23] and Trofimov et al. [24]) use the *Abaqus* subroutine ORIENT to determine the orientation vector according to the deposition trajectory. In this method, implemented in the *Abaqus AM Modeler* [15], the orientation vector is fixed once based on the initial volume fraction deposited in each element and does not update when subsequent material with differing orientation is added. This means, for example, that a component with alternating infill directions of 0°/90° effectively exhibits unidirectional material properties (e.g., entirely 0°). As a result, the actual combination of orientations within the element is neglected. This simplification can lead to significant errors in predicting stiffness and deformation behavior. Moreover, this approach is limited because it uses a single orientation vector rather than a full orientation tensor, restricting the representation of complex material orientations.

In summary, while various FE-based approaches exist for simulating PiD in MEX components, the evolving mesostructure and resulting anisotropic material behavior during the process are either oversimplified or neglected. This gap highlights a critical need for improved models that accurately capture material anisotropy to enhance prediction fidelity in MEX process simulations.

Since the local mesostructure plays a key role in determining the final performance of MEX components, several studies have investigated characteristic mesostructures within structural simulations to derive stiffness properties. The main modeling strategies in this context are therefore reviewed and assessed for their suitability in process simulations aimed at predicting PiD. Existing research in this field primarily focuses on representing the anisotropic mechanical behavior and stiffness of MEX components through multiscale modeling. Commonly used techniques include homogenization based on classical laminate theory (CLT) [25–28], representative volume elements (RVEs) [29–31], hybrid CLT-RVE methods [32], and fast fourier transformation (FFT)-based homogenization [33].

CLT determines effective elastic properties by treating individual layers of a MEX component as laminates and calibrating the stiffness matrix using unidirectional experimental data [25–28]. Nevertheless, one major drawback of this method is its limited accuracy in capturing variations in material behavior across the full thickness of each layer.

Homogenized models utilizing RVEs are capable of replicating the macroscopic behavior of components with structured infill geometries [29–31]. Despite this, their implementation in FEM-based process simulations is constrained, particularly when simulating element activation, evolving mesostructures, and transient thermal fields. To reflect the true effective properties at every location during the process, a distinct RVE analysis is needed for each point experiencing different temperatures and structural configurations. This necessitates continuous RVE recalculations throughout the simulation, resulting in a high computational effort that makes real-time simulations with element activation practically unfeasible.

FFT-based homogenization is a computationally efficient method for capturing anisotropic properties and spatial variations in MEX components. Liu et al. [33] modeled extrusion-path-dependent behavior using a rotated transversely isotropic material model. However, in process simulations, the method must be recalculated frequently to reflect evolving temperatures and mesostructures, which leads to high overall computational cost. Additionally, integration into conventional FEM tools like *Abaqus* is challenging, so such methods are typically implemented in custom simulation frameworks.

In summary, these homogenization methods require substantial numerical or experimental effort and are not yet practical for efficient PiD prediction in MEX process simulations, revealing a significant research gap.

A common method to more comprehensively describe material orientation in inhomogeneous structures involves the use of second- and fourth-order orientation tensors [34,35]. These orientation tensors represent the statistical distribution of fiber or grain orientations within a volume. The second-order orientation tensor characterizes the preferred direction of material orientation and indicates whether the distribution is anisotropic or isotropic. It captures the mean orientation but lacks information about the spread or variability around this direction. In contrast, the fourth-order orientation tensor provides a more detailed description of the orientation distribution. It accounts not only for the preferred direction but also for the degree of dispersion around it. This allows for a more accurate determination of anisotropic material properties such as stiffness and thermal expansion. By averaging the orientation distribution over the volume, effective material properties, such as stiffness tensors, can be computed [35].

1.2. Originality

This work addresses the central research gap outlined above: the integration of process-specific, inhomogeneous mesostructures into full-scale FE simulations of the MEX process for predicting PiD. The main challenge is to accurately capture local anisotropic effects while maintaining computational efficiency through appropriate discretization strategies.

To this end, the paper presents a novel anisotropic homogenization method that accounts for the characteristic inhomogeneous mesostructure of the MEX process. The approach builds on the orientation averaging scheme [35], adapted to reflect MEX-specific features. Key modifications to the formulation of orientation tensors and the averaging procedure are introduced, along with details of the numerical implementation. The fundamental idea of representing the material orientation of the mesostructure with orientation tensors was first proposed by us in [36]. This work builds on the basic framework introduced in [36] by formulating and implementing it efficiently for arbitrary component geometries and real G-Code data.

The implementation is verified, and the overall simulation strategy is validated against experimental data. A comparison with an equivalent isotropic approach highlights the relevance of including local mesostructural effects. Additional numerical studies investigate the evolution of effective material orientation during processing and in the final printed component.

The key contributions of this study can be summarized as follows:

- Description and categorization of the MEX-typical mesostructure.
- Formulation of the homogenization approach based on orientation averaging. This includes the formulation of orientation tensors and the orientation averaging to determine the effective stiffnesses based on an experimentally determined orthotropic stiffness tensor.
- Implementation of the homogenization approach, considering process-typical special cases for application in the FE software *Abaqus*.
- Verification of the approach and the implementation in *Python* and *Abaqus*.

- Numerical studies using the ansiotropic homogenization approach to investigate local material orientation during the printing process.
- Formulation of an equivalent isotropic approach that derives an isotropic description from the experimentally determined orthotropic stiffness.
- Experimental validation of the anisotropic homogenization approach based on experiments. For this purpose, the characterization of the PLA used as an example is discussed and the experiment is presented.
- Comparison of measured deformation with anisotropic and equivalent isotropic stiffness descriptions.

1.3. Notation

$\mathbb{A}[\boldsymbol{B}]$	Mapping of a 2nd-order tensor by a 4th-order tensor, i.e. $(\mathbb{A}[\boldsymbol{B}])_{ij} = A_{ijkl}B_{kl}$
$\mathrm{tr}\,\bullet$	Trace, e.g. $\mathrm{tr}\,\mathbf{A} = A_{ii}$
$\|\bullet\|$	Frobenius norm, e.g. $\|\mathbf{A}\| = \sqrt{\mathbf{A} : \mathbf{A}}$
$\cdot$	Scalar product, e.g. $\mathbf{A} \cdot \mathbf{B} = A_{ij}B_{ij}$
$:$	Frobenius scalar product (double trace product or trace product), e.g. $\mathbf{A} : \mathbf{B} = \sum_{i,j} A_{ij}B_{ij}$
$\otimes$	Dyadic product, e.g. $\mathbf{n} \otimes \mathbf{n} = n_i n_j$
$\square$	Product between second-order tensors: $(\mathbf{A} \square \mathbf{C})\mathbf{B} = A_{ik}B_{kl}C_{lj}$
$\star$	Rayleigh product: $\mathbf{Q} \star \mathbf{A} = \mathbf{Q}\mathbf{A}\mathbf{Q}^{\top}$ with $\boldsymbol{Q} \in \mathrm{Orth}^{+}$
$(\bullet)^{n\otimes}$	Dyadic product repeated n times to form an nth-order tensor
$\langle\bullet\rangle_S$	Averaging over surface S

2. Homogenization approach

2.1. Description of the mesostructure

Components manufactured by using MEX can generally be divided into three distinct mesostructural regions:

1. The perimeter area, which defines the contour of the component.
2. The infill, which can be freely specified.
3. The transition zone between the perimeter and the infill, where changes in the extrusion nozzle's movement direction result in a modified mesostructure.

The infill pattern is defined by various parameters, including the infill angle, which controls the orientation of the deposited strands. Both the infill and the number of perimeters can be defined prior to fabrication, allowing for a wide range of local mesostructures within the same component geometry and material density. Fig. 1 schematically illustrates the three regions described. In addition to the orientation of the deposited strands, the mesostructure is also characterized by the resulting voids. Fig. 2 shows a resulting mesostructure of an infill area for a print in which all strands are deposited in the same direction. A schematic representation (left) and a microscopic image (right) is shown.

The local mesostructure strongly contributes to the stiffness of the component and thus directly controls the PiD of the manufactured component. Throughout this paper, the coordinate system shown in Fig. 2 will be used. An extrusion in the x-direction is defined as an infill angle of 0°, and an extrusion in the y-direction is defined as an infill angle of 90°. It should be noted that the mesostructures within the three categories "Perimeter", "Perimeter + Infill + Turning points", and "Infill" scatter in the real process and are not exactly identical throughout the component. The approach presented in this paper neglects this process scatter.

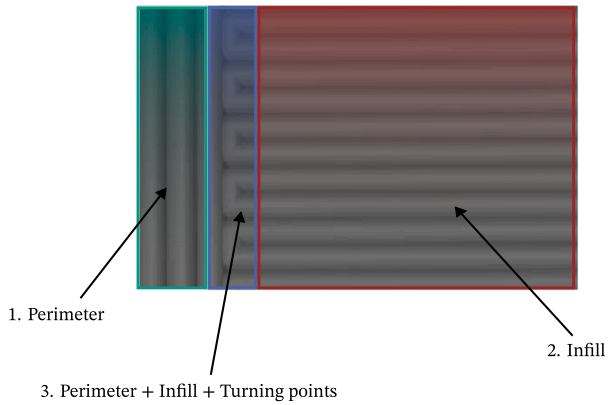

Fig. 1. Classification of process-typical mesostructures into three different categories: perimeter (green), infill (red) and the area between perimeter and infill defined by the turning points of the extrusion and parts of the infill (blue).

2.2. Anisotropic approach

To homogenize the resulting mesostructure, the orientation average scheme is used in this work [35]. It is used to determine the statistical distribution of the orientation of particles or fibers (e.g., in suspensions or composites) and to derive effective macroscopic properties.

This approach is applied to the MEX process to determine the influence of the process-typical complex and directional mesostructure on the macroscopic properties of the additively manufactured component. The orientation formulation is based on the following assumptions:

- The properties of the resulting material are considered as a function of the spatial distribution and orientation of its phases (extruded strand and air).
- Periodic mesostructures are assumed.

The orientation distribution function (ODF) $f(\boldsymbol{x}, \boldsymbol{p})$ is used to describe the resulting mesostructures statistically [35]. This function represents a probability density. Its integration yields the probability of finding an extruded strand aligned in the direction $\boldsymbol{p}$ at the spatial position $\boldsymbol{x}$. $f(\boldsymbol{x}, \boldsymbol{p})$ is characterized by the following properties:

$$f(\boldsymbol{x}, \boldsymbol{p}) \geq 0, \qquad f(\boldsymbol{x}, \boldsymbol{p}) = f(\boldsymbol{x}, -\boldsymbol{p}), \qquad \int_{S^2} f(\boldsymbol{x}, \boldsymbol{p}) \mathrm{d}S = 1. \tag{1}$$

The surface of the unit sphere is denoted by S^2 with the surface element dS. In a simplified form, the value of ODF $f_m(\boldsymbol{x}, \boldsymbol{p}_m)$ represents the orientation fraction of material m in position $\boldsymbol{x}$ with orientation $\boldsymbol{p}_m$. In the context of MEX, the orientation $\boldsymbol{p}$, the position $\boldsymbol{x}$, and the extrusion rate are given by the G-Code. The function $f_m(\boldsymbol{x}, \boldsymbol{p}_m)$ can therefore be defined as the volume fraction of strand m with orientation $\boldsymbol{p}_m$ within a volume (e.g. finite element) at position $\boldsymbol{x}$. For a total of N extruded strands contributing to the volume, this is expressed as:

$$f_m(\boldsymbol{x}, \boldsymbol{p}_m) = \frac{V_m(\boldsymbol{x}, \boldsymbol{p}_m)}{\sum_{i=1}^{N} V_i(\boldsymbol{x}, \boldsymbol{p}_i)} \tag{2}$$

where V_m is the volume of strand m within the considered volume, and the denominator represents the total volume of all strands intersecting that volume. Owing to the characteristics of the standard MEX process, the extruded strands are confined to the x–y plane, with no out-of-plane (z-direction) orientation (see Appendix A for a discussion on 3D deposition paths). For this planar orientation, $\theta = \pi/2$ applies to all strands, and each orientation state is described by the angle ϕ, as illustrated in Fig. 3.

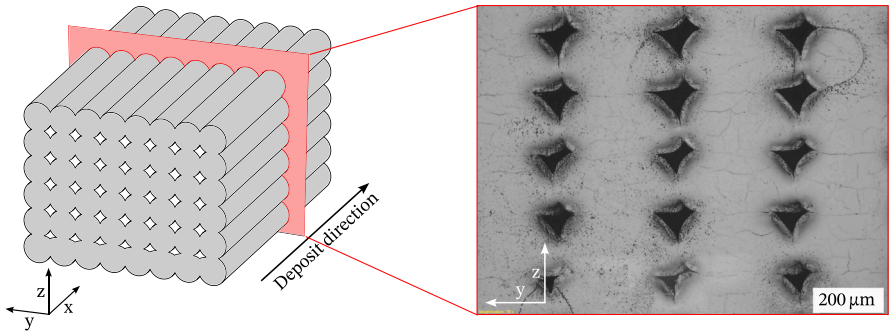

Fig. 2. Schematic representation of a unidirectionally printed mesostructure and microscopic image of the cross-section in the y–z plane.

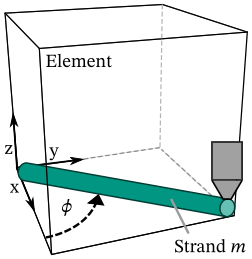

Fig. 3. Illustration of a deposited strand m with orientation angle ϕ within a finite element, considered as the control volume for homogenization.

Therefore, the orientation vector $\boldsymbol{p}_m$ of each strand m can be described as

$$\boldsymbol{p}_m = \begin{bmatrix} p_x \\ p_y \\ p_z \end{bmatrix}_m = \begin{bmatrix} \cos(\phi) \\ \sin(\phi) \\ 0 \end{bmatrix}_m . \tag{3}$$

The orientation space is therefore not a sphere, as in the case of arbitrary spatial orientations, but rather a circle due to the restriction to the 1–2 plane.

An averaged description of the state of orientation can be obtained using orientation tensors (OT), where the second-order tensor $\boldsymbol{A}$ and the fourth-order tensor $\mathbb{A}$ are used in practice [35]:

$$\boldsymbol{A} = \int_{S^2} f(\boldsymbol{x},\boldsymbol{p})\boldsymbol{p}\otimes\boldsymbol{p}\,\mathrm{d}S, \qquad \mathbb{A} = \int_{S^2} f(\boldsymbol{x},\boldsymbol{p})\boldsymbol{p}\otimes\boldsymbol{p}\otimes\boldsymbol{p}\otimes\boldsymbol{p}\,\mathrm{d}S. \tag{4}$$

The tensors must fulfill the following requirements:

$$\boldsymbol{A} = \boldsymbol{A}^{\mathsf{T}}, \qquad \mathrm{tr}\boldsymbol{A} = 1, \qquad \mathbb{A}[\boldsymbol{I}] = \boldsymbol{A} \tag{5}$$

Using Eq. (2), the orientation tensors $\boldsymbol{A}$ and $\mathbb{A}$ can be approximated by the following normalized expression for a mesostructure with N strands:

$$\boldsymbol{A} = \sum_{m=1}^{N} \left(\frac{V_m}{\sum_{i=1}^{N} V_i} \right) (\boldsymbol{p}\otimes\boldsymbol{p})_m \tag{6}$$

$$\mathbb{A} = \sum_{m=1}^{N} \left(\frac{V_m}{\sum_{i=1}^{N} V_i} \right) (\boldsymbol{p}\otimes\boldsymbol{p}\otimes\boldsymbol{p}\otimes\boldsymbol{p})_m \tag{7}$$

Unlike the standard procedures used in most other process simulations (such as injection molding), this procedure allows for the explicit calculation of the 4th-order OT, rather than approximating it using a closure. This has the advantage that uncertainties associated with the closure are not transferred to the effective mechanical properties [37,38]. As the mesostructure within a given element evolves during the printing process, the orientation tensors $\boldsymbol{A}$ (second-order) and $\mathbb{A}$ (fourth-order) become time-dependent. They are therefore computed at each time increment t_i, based on the updated strand orientation at the end of the increment.

To determine a valid macroscopic effective stiffness $\bar{\mathbb{C}}$ of the additively manufactured component, orientation averaging is performed over all strand directions in the mesostructure. This approach is based on the orientation averaging framework introduced by Advani and Tucker [35], which was originally developed for discontinuous fiber-reinforced composites. In the context of MEX printing, the framework is adapted to account for the layer by layer nature of the MEX mesostructure. A key characteristic of the standart MEX process is that the third orthotropic material axis, $\boldsymbol{e}_3$, is always aligned with the global build direction ($[0,0,1]^{\mathsf{T}}$). As a result, the orientation averaging emphasizes the in-plane variation of strand orientations, represented by the second- and fourth-order orientation tensors $\boldsymbol{A}$ and $\mathbb{A}$. The following derivation presents the orientation averaging procedure specifically tailored to this MEX-specific case.

The effective stiffness tensor $\bar{\mathbb{C}}$ is defined as a Voigt-like average:

$$\bar{\mathbb{C}} := \langle \mathbb{C} \rangle_S = \int_{S^2} \mathbb{C}(\boldsymbol{p}) f(\boldsymbol{x},\boldsymbol{p})\mathrm{d}S, \tag{8}$$

where $\mathbb{C}(\boldsymbol{p})$ is already an effective (homogenized) stiffness tensor associated with strands oriented in direction $\boldsymbol{p}$, and $f(\boldsymbol{x},\boldsymbol{p})$ is the orientation distribution function. The goal is to express $\bar{\mathbb{C}}$ in terms of the orientation tensors and material parameters:

$$\bar{\mathbb{C}} = f\left(\mathbb{A}, \boldsymbol{A}, \boldsymbol{p}\right). \tag{9}$$

The derivation begins with hyperelasticity theory, where stresses $\boldsymbol{\sigma}$ are obtained as the derivative of a strain energy density function $w(\boldsymbol{\varepsilon})$. For a linear stress–strain relationship, the strain energy function $w(\boldsymbol{\varepsilon})$ must be quadratic in $\boldsymbol{\varepsilon}$:

$$\begin{aligned} w(\boldsymbol{\varepsilon}) = &\frac{a}{2}\varepsilon_{11}^2 + \frac{b}{2}\varepsilon_{22}^2 + \frac{c}{2}\varepsilon_{33}^2 + d\varepsilon_{11}\varepsilon_{22} + e\varepsilon_{11}\varepsilon_{33} + f\varepsilon_{22}\varepsilon_{33} + 2g\varepsilon_{23}^2 \\ &+ 2h\varepsilon_{13}^2 + 2p\varepsilon_{12}^2 \end{aligned} \tag{10}$$

with nine independent material coefficients a to p.

The symmetric dyadic product is used for the strain basis tensors:

$$\boldsymbol{K}_{ij} = \frac{1}{2}\left(\boldsymbol{e}_i\otimes\boldsymbol{e}_j + \boldsymbol{e}_j\otimes\boldsymbol{e}_i\right), \tag{11}$$

which satisfies:

$$\boldsymbol{K}_{ij} : \boldsymbol{\varepsilon} = \varepsilon_{ij}, \quad \text{so that} \quad \boldsymbol{K}_{ij} = \frac{\partial \varepsilon_{ij}}{\partial \boldsymbol{\varepsilon}}. \tag{12}$$

From this, the stiffness tensor is:

$$\begin{aligned} \mathbb{C} := \frac{\partial^2 w(\boldsymbol{\varepsilon})}{\partial \boldsymbol{\varepsilon}^2} = \frac{\partial \boldsymbol{\sigma}}{\partial \boldsymbol{\varepsilon}} = &a\boldsymbol{K}_{11}\otimes\boldsymbol{K}_{11} + b\boldsymbol{K}_{22}\otimes\boldsymbol{K}_{22} + c\boldsymbol{K}_{33}\otimes\boldsymbol{K}_{33} \\ &+ d(\boldsymbol{K}_{11}\otimes\boldsymbol{K}_{22} + \boldsymbol{K}_{22}\otimes\boldsymbol{K}_{11}) \\ &+ e(\boldsymbol{K}_{11}\otimes\boldsymbol{K}_{33} + \boldsymbol{K}_{33}\otimes\boldsymbol{K}_{11}) \\ &+ f(\boldsymbol{K}_{22}\otimes\boldsymbol{K}_{33} + \boldsymbol{K}_{33}\otimes\boldsymbol{K}_{22}) \\ &+ 4g\boldsymbol{K}_{23}\otimes\boldsymbol{K}_{23} + 4h\boldsymbol{K}_{13}\otimes\boldsymbol{K}_{13} \\ &+ 4p\boldsymbol{K}_{12}\otimes\boldsymbol{K}_{12}. \end{aligned} \tag{13}$$

The orthotropic basis vectors in the context of MEX, as shown in Fig. 3, can be defined:

$$\boldsymbol{e}_1 = \begin{bmatrix} \cos(\phi) \\ \sin(\phi) \\ 0 \end{bmatrix} = \boldsymbol{p} \qquad \boldsymbol{e}_2 = \begin{bmatrix} -\sin(\phi) \\ \cos(\phi) \\ 0 \end{bmatrix} = \boldsymbol{p}_\perp \qquad \boldsymbol{e}_3 = \begin{bmatrix} 0 \\ 0 \\ 1 \end{bmatrix}. \tag{14}$$

With Eq. (11), this gives

$$\boldsymbol{K}_{ij} = \mathrm{sym}\left(\begin{bmatrix} \boldsymbol{p}\otimes\boldsymbol{p} & \boldsymbol{p}\otimes\boldsymbol{p}_\perp & \boldsymbol{p}\otimes\boldsymbol{e}_3 \\ \boldsymbol{p}_\perp\otimes\boldsymbol{p} & \boldsymbol{p}_\perp\otimes\boldsymbol{p}_\perp & \boldsymbol{p}_\perp\otimes\boldsymbol{e}_3 \\ \boldsymbol{p}\otimes\boldsymbol{p} & \boldsymbol{p}\otimes\boldsymbol{p}_\perp & \boldsymbol{e}_3\otimes\boldsymbol{e}_3 \end{bmatrix} \right). \tag{15}$$

From these, the $\boldsymbol{K}_{ij}$ tensors are constructed and averaged over the orientation space. The results can be expressed in terms of the orientation tensors $\boldsymbol{A}$ and $\mathbb{A}$, along with the planar identity tensor $\boldsymbol{I}^{\mathrm{pl}} = \boldsymbol{e}_1^2 + \boldsymbol{e}_2^2$, and the dyadic products involving $\boldsymbol{e}_3$. This leads to analytical expressions for the orientation-averaged components $\langle \boldsymbol{K}_{ij} \otimes \boldsymbol{K}_{kl} \rangle_S$, as follows:

$$\langle \boldsymbol{K}_{11} \otimes \boldsymbol{K}_{11} \rangle_S = \langle \boldsymbol{p}^{4\otimes} \rangle_S = \mathbb{A} \tag{16a}$$

$$\langle \boldsymbol{K}_{22} \otimes \boldsymbol{K}_{22} \rangle_S = \boldsymbol{I}^{\mathrm{pl}} \otimes \boldsymbol{I}^{\mathrm{pl}} - \boldsymbol{I}^{\mathrm{pl}} \otimes \boldsymbol{A} - \boldsymbol{A} \otimes \boldsymbol{I}^{\mathrm{pl}} + \mathbb{A} \tag{16b}$$

$$\langle \boldsymbol{K}_{33} \otimes \boldsymbol{K}_{33} \rangle_S = \langle \boldsymbol{e}_3^{4\otimes} \rangle_S = \boldsymbol{e}_3^{4\otimes} \tag{16c}$$

$$\langle \boldsymbol{K}_{11} \otimes \boldsymbol{K}_{22} + \boldsymbol{K}_{22} \otimes \boldsymbol{K}_{11} \rangle_S = \boldsymbol{I}^{\mathrm{pl}} \otimes \boldsymbol{A} + \boldsymbol{A} \otimes \boldsymbol{I}^{\mathrm{pl}} - 2\mathbb{A} \tag{16d}$$

$$\langle \boldsymbol{K}_{11} \otimes \boldsymbol{K}_{33} + \boldsymbol{K}_{33} \otimes \boldsymbol{K}_{11} \rangle_S = \boldsymbol{A} \otimes \boldsymbol{e}_3^{2\otimes} + \boldsymbol{e}_3^{2\otimes} \otimes \boldsymbol{A} \tag{16e}$$

$$\langle \boldsymbol{K}_{22} \otimes \boldsymbol{K}_{33} + \boldsymbol{K}_{33} \otimes \boldsymbol{K}_{22} \rangle_S = \boldsymbol{I}^{\mathrm{pl}} \otimes \boldsymbol{e}_3^{2\otimes} + \boldsymbol{e}_3^{2\otimes} \otimes \boldsymbol{I}^{\mathrm{pl}} - \boldsymbol{A} \otimes \boldsymbol{e}_3^{2\otimes} - \boldsymbol{e}_3^{2\otimes} \otimes \boldsymbol{A} \tag{16f}$$

$$\langle \boldsymbol{K}_{13} \otimes \boldsymbol{K}_{13} \rangle_S = \frac{1}{4} \left(\boldsymbol{A} \square \boldsymbol{e}_3^{2\otimes} + \left(\boldsymbol{A} \square \boldsymbol{e}_3^{2\otimes} \right)^{\top_R} + \boldsymbol{e}_3^{2\otimes} \square \boldsymbol{A} + \left(\boldsymbol{e}_3^{2\otimes} \square \boldsymbol{A} \right)^{\top_R} \right) \tag{16g}$$

$$\langle \boldsymbol{K}_{12} \otimes \boldsymbol{K}_{12} \rangle_S = \frac{1}{4} \left(\boldsymbol{A} \square \boldsymbol{I}^{\mathrm{pl}} + \left(\boldsymbol{A} \square \boldsymbol{I}^{\mathrm{pl}} \right)^{\top_R} \right. \tag{16h}$$

$$\left. + \boldsymbol{I}^{\mathrm{pl}} \square \boldsymbol{A} + \left(\boldsymbol{I}^{\mathrm{pl}} \square \boldsymbol{A} \right)^{\top_R} \right) - \mathbb{A} \tag{16i}$$

$$\langle \boldsymbol{K}_{23} \otimes \boldsymbol{K}_{23} \rangle_S = \frac{1}{4} \left(\boldsymbol{I}^{\mathrm{pl}} \square \boldsymbol{e}_3^{2\otimes} + \left(\boldsymbol{I}^{\mathrm{pl}} \square \boldsymbol{e}_3^{2\otimes} \right)^{\top_R} \right. \tag{16j}$$

$$- \boldsymbol{A} \square \boldsymbol{e}_3^{2\otimes} - \left(\boldsymbol{A} \square \boldsymbol{e}_3^{2\otimes} \right)^{\top_R}$$

$$+ \boldsymbol{e}_3^{2\otimes} \square \boldsymbol{I}^{\mathrm{pl}} + \left(\boldsymbol{e}_3^{2\otimes} \square \boldsymbol{I}^{\mathrm{pl}} \right)^{\top_R}$$

$$\left. - \boldsymbol{e}_3^{2\otimes} \square \boldsymbol{A} - \left(\boldsymbol{e}_3^{2\otimes} \square \boldsymbol{A} \right)^{\top_R} \right).$$

With Eqs. (6), (7), (13), and (16), the effective stiffness tensor $\bar{\mathbb{C}}$ of the MEX-printed mesostructure can be expressed as a function of the second- and fourth-order orientation tensors $\boldsymbol{A}$ and $\mathbb{A}$. The material-specific coefficients a to p in Eq. (13) are obtained directly from experimental characterization of the unidirectionally printed orthotropic material, represented by the stiffness tensor $\mathbb{C}^{\mathrm{exp}}_{\mathrm{ortho}}$.

2.2.1. Implementation

The implementation relies on custom *Python* scripts and *Abaqus* subroutines to calculate the effective stiffness $\bar{\mathbb{C}}$, which evolves during the process, in each finite element. This calculation is based on the strands deposited during the manufacturing process and their orientation $\boldsymbol{p}$ within each element during the simulation. The input data consists of G-Code, generated by standard slicing software. This G-Code is processed using the open-source *Python* package *pyGCodeDecode* (*pyGCD*) [39,40], which extracts the necessary event series for the process simulation in *Abaqus*. This package [40] enables precise reconstruction of the nozzle trajectory, accounting for the printer's firmware, as well as its specific settings and limitations. The process is summarized in Fig. 4, and the steps are described in detail below.

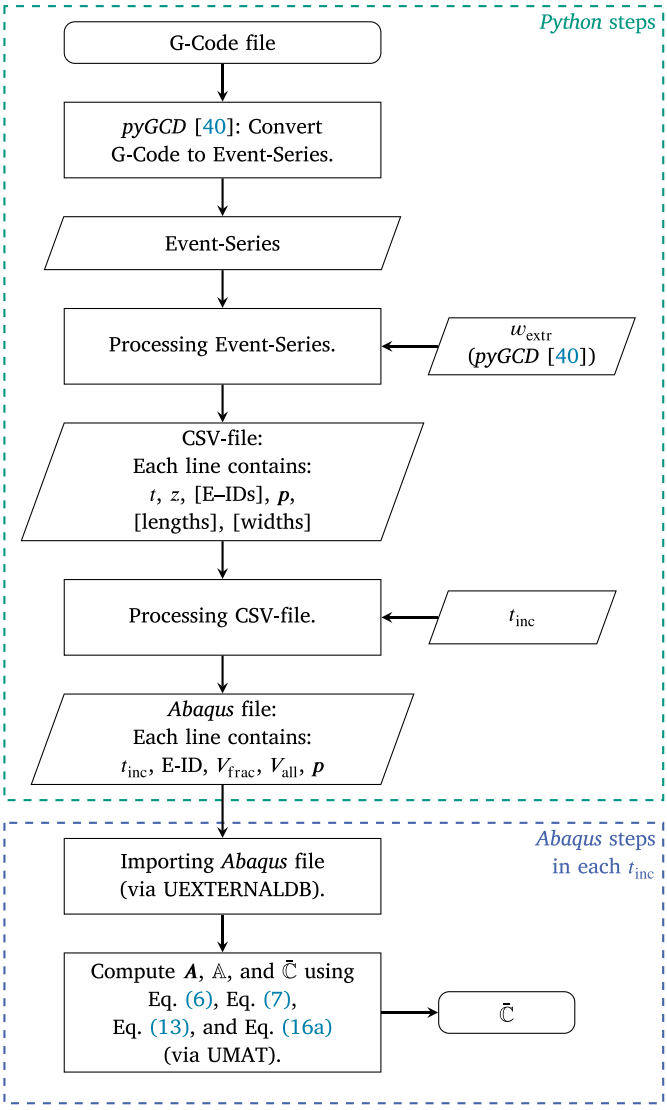

Fig. 4. Flowchart of the implemented workflow for the computation of orientation tensors $\boldsymbol{A}$ and $\mathbb{A}$ and the corresponding effective stiffness $\bar{\mathbb{C}}$ in each element at every time increment.

Processing Event-Series. In the next step of the algorithm, the generated event series is processed line by line. For each event, it is determined which finite elements are intersected by the corresponding nozzle motion. Only movements associated with material extrusion are taken into account. To minimize computational effort, the centroids of all elements are organized in a kd-tree structure, enabling an efficient search within the current nozzle height level. This allows restricting the search to the eight elements surrounding the element currently occupied by the nozzle, thereby significantly reducing the number of intersection checks. The underlying search uses a k-nearest neighbor (kNN) approach as a practical tool to achieve this efficiency. As a result, the algorithm remains computationally efficient even for components with a large number of elements.

When analyzing nozzle motion within an element, several relevant scenarios must be considered to accurately map the extrusion process onto the mesh. The scenarios are listed below and illustrated in Fig. 5:

(a) Both the start point (1) and the end point (2) of the nozzle motion lie outside the element.

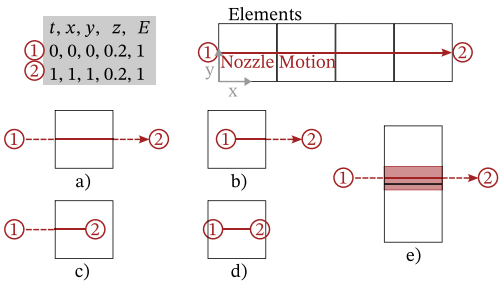

Fig. 5. Representation of a nozzle motion (1 → 2) as it passes through elements. As well as the considered scenarios for such a nozzle motion (a–e).

(b) The start point (1) lies inside the element, while the end point (2) lies outside.
(c) The start point (1) lies outside the element, while the end point (2) lies inside.
(d) Both the start point (1) and the end point (2) lie inside the element.
(e) The extruded strand spans across two adjacent elements.

For each element in which a strand is deposited, the respective length of the nozzle motion, the width of the deposited strand, and the orientation vector $\boldsymbol{p}$ according to Eq. (3) are also determined. For the width of the deposited strand, *pyGCD* is used to calculate the average extrusion width from the G-Code during the analyzed nozzle motion. The orientation is defined with regard to the x-axis (1-direction). The information with the according Element-IDs (E-IDs) are stored in a CSV-file for each motion. The structure is shown in Fig. 5. This information can then be used to calculate and interpret the resulting orientation tensors at specific times during the process.

Processing CSV-file. The information in the CSV-file is further interpreted for use in *Abaqus*. For a given time increment t_{inc} from the subsequent process simulation, the algorithm evaluates how many strands with a certain orientation $\boldsymbol{p}$ are deposited in which element (E-ID). For each time increment and each element, the strands with the same orientation are grouped. In addition, their volume fraction V_{frac} in the element and the total volume V_{all} deposited in the element up to this time increment are stored in a file.

Importing Abaqus file. At the start of the process simulation, a user subroutine UEXTERNALDB reads the file and stores the information in global arrays. In this way, the file only needs to be read once per simulation.

Compute $\boldsymbol{A}$, $\mathbb{A}$, *and* $\bar{\mathbb{C}}$. The material model used in the simulation (see Section 3.1.2) is implemented as a user subroutine UMAT. Within this UMAT, which is called for each integration point in each time increment, the information in the global arrays is accessed. For each element, the orientation tensors $\boldsymbol{A}$ and $\mathbb{A}$ are calculated here in each time increment using Eqs. (6) and (7). Eqs. (13) and (16) then provide $\bar{\mathbb{C}}$. If no strand is added to the element in the current time increment, $\boldsymbol{A}$, $\mathbb{A}$, and $\bar{\mathbb{C}}$ are not recalculated. $\bar{\mathbb{C}}$ is then the starting point for the further material model, which is described in Section 3.1.2.

2.2.2. Verification

To verify the implemented workflow, a plate with dimensions of 27 mm × 27 mm × 1 mm and elements with dimensions of 9 mm × 9 mm × 1 mm is analyzed. Based on the G-Code generated for each case, the *Abaqus* file was created according to the procedure described in Section 2.2.1. The implemented *Abaqus* subroutines were then used to calculate the orientation tensors and volume fraction for the example geometry. An extrusion width of 3 mm and different trajectories were considered to cover different cases, as illustrated in Fig. 6. The dimensions of the component and its discretization allow an easy comparison of the volume fractions and a direct evaluation of the results of the implemented subroutines. To verify the calculated orientation of each element, the planar fractional anisotropy given by

$$a_{\text{fr}}^{\text{pl}} = \sqrt{\frac{8}{5}} \frac{\|\mathbb{A}_{\text{pl}} - \mathbb{A}_{\text{pl}}^{\text{iso}}\|}{\|\mathbb{A}_{\text{pl}}\|} \tag{17}$$

is used. Here $\mathbb{A}_{\text{pl}}$ is the planar fourth-order orientation tensor and $\mathbb{A}_{\text{pl}}^{\text{iso}}$ is its isotropic fraction. This provides a scalar comparison value for the orientation. Here, $a_{\text{fr}}^{\text{pl}} = 0$ stands for planar isotropy in the x–y plane and $a_{\text{fr}}^{\text{pl}} = 1$ for unidirectional orientation. Fig. 6 shows the corresponding calculated orientations and volume fractions in the nine elements of the component with *Abaqus*. The results show that the resulting orientation and volume fraction are correctly assigned to the individual elements for all cases described in Section 2.2.1. The resulting volume fraction is easy to calculate, except for the fourth case, and can therefore be easily checked. Since this is not the case in the fourth case, the information on the volume fraction has been omitted here, but checked by an analytical calculation using *Python*.

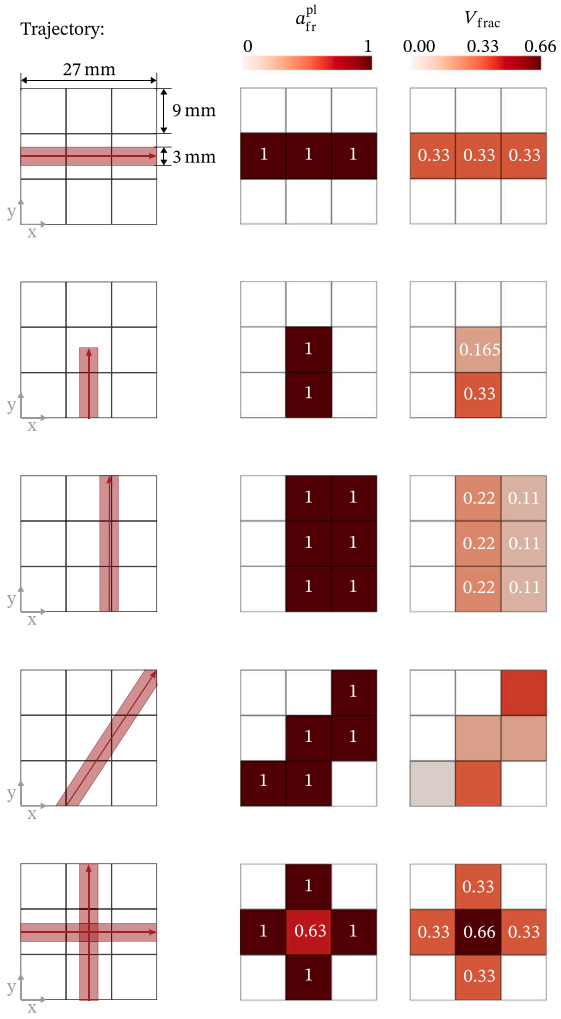

Fig. 6. Analyzed trajectories and the corresponding planar fractional anisotropy $a_{\text{fr}}^{\text{pl}}$ and volume fractions V_{frac} in the nine elements of the component used to verify the implemented workflow from Fig. 4 within *Abaqus*.

2.2.3. Numerical studies of the resulting material orientation

To analyze the resulting material orientation in additively manufactured components during and at the time of completion, a plate measuring 48 mm × 48 mm × 2.4 mm was examined. The component was sliced with three perimeters and alternating 0° and 90° infill. The strand width was 0.4 mm and the height was 0.2 mm. To demonstrate the influence of the element size, hexahedral elements with edge lengths of 0.6 mm, 0.8 mm, 1.2 mm and 2.4 mm in all three spatial directions were examined. The following figures in this section show the details of the plate with the respective discretization and the planar fractional anisotropy $a_{\mathrm{fr}}^{\mathrm{pl}}$ according to Eq. (17).

Fig. 7(a) shows the resulting orientation states at the end of the component production. A visualization plot of the planar fourth-order orientation tensor $\mathbb{A}_{\mathrm{pl}}$ using so-called HOME-glyphs [41] is shown for different locations within the component. It represents the in-plane orientation of the material in the x–y plane. The $a_{\mathrm{fr}}^{\mathrm{pl}}$ of each element shows the uniformly distributed infill mesostructure in the center of the component. Due to the element size, the "Perimeter" and "Perimeter + Infill + Turning points" mesostructures are combined. The visualization plots reveal a pronounced alignment of the material in the outer areas of the component. This is due to the perimeters and turning points. Such a prediction is plausible given the actual material orientation in the component.

Fig. 7(b) shows the evolution of $a_{\mathrm{fr}}^{\mathrm{pl}}$ throughout the process time at different points in the component.The progression of the orientation after printing the first strand in the respective element is shown. It can be seen that although the same material orientation is partially reached at the end, the orientation evolves differently during the printing process. The time dependence of the material orientation is due to the alternating infill. As a result, alternating orientations of the extruded material are added during the process until the element is completely filled with strands. These results show that the component has locally different stiffness during the printing process, which affects the PiD. This study demonstrates that the presented approach can capture the evolving material orientation within an individual element, thereby representing a significant advancement beyond the fixed-orientation approach currently available in *Abaqus*. To achieve an identical stiffness evolution (apart from the influence of perimeters

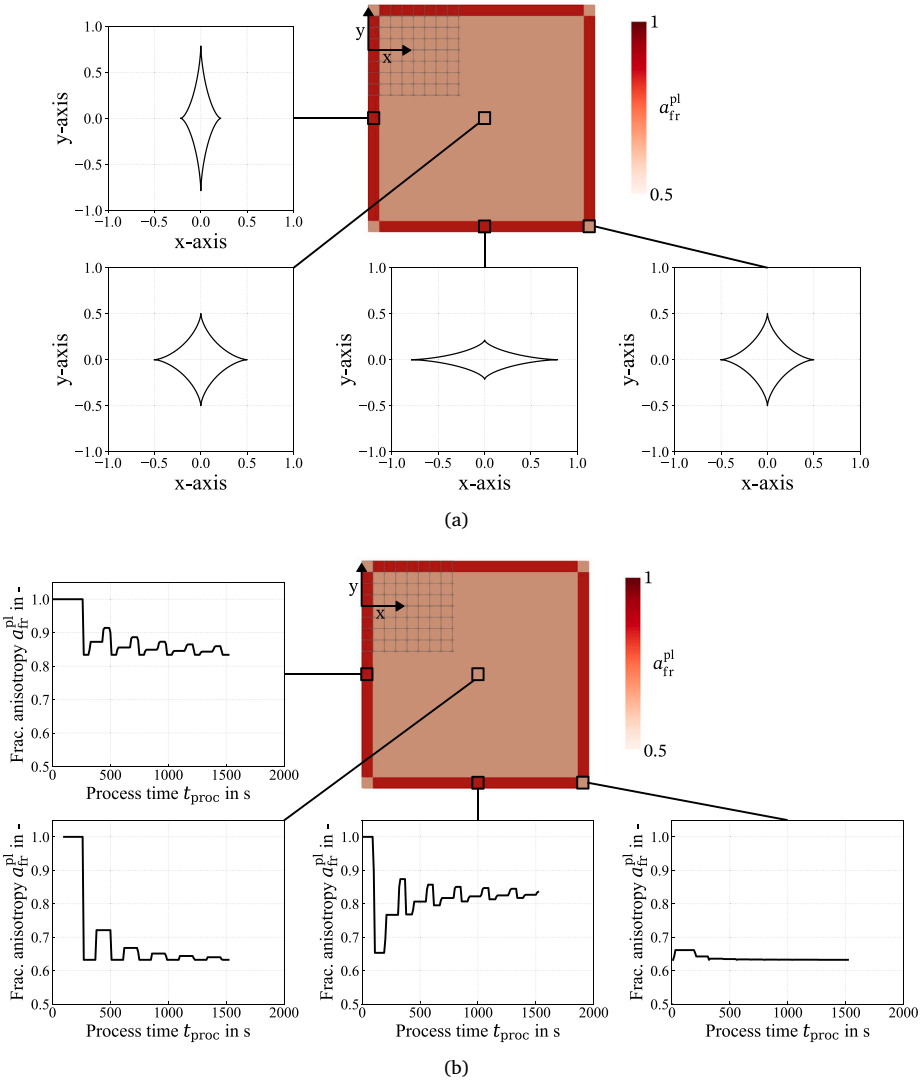

Fig. 7. (a) Visualization of the planar fourth-order orientation tensor $\mathbb{A}_{\mathrm{pl}}$ at different locations within the component. The component is discretized using elements with edge lengths of 2.4 mm in all three spatial directions. The plot illustrates the in-plane orientation of the material in the x–y plane, showing a uniform mesostructure in the center and a pronounced alignment in the outer regions due to perimeters and turning points of the extrusion. (b) Evolution of $a_{\mathrm{fr}}^{\mathrm{pl}}$ over the process time at different points in the component. The plots illustrate the evolution of the material orientation, showing time-dependent variations due to alternating infill. The printing time for one layer is approximately 200 s.

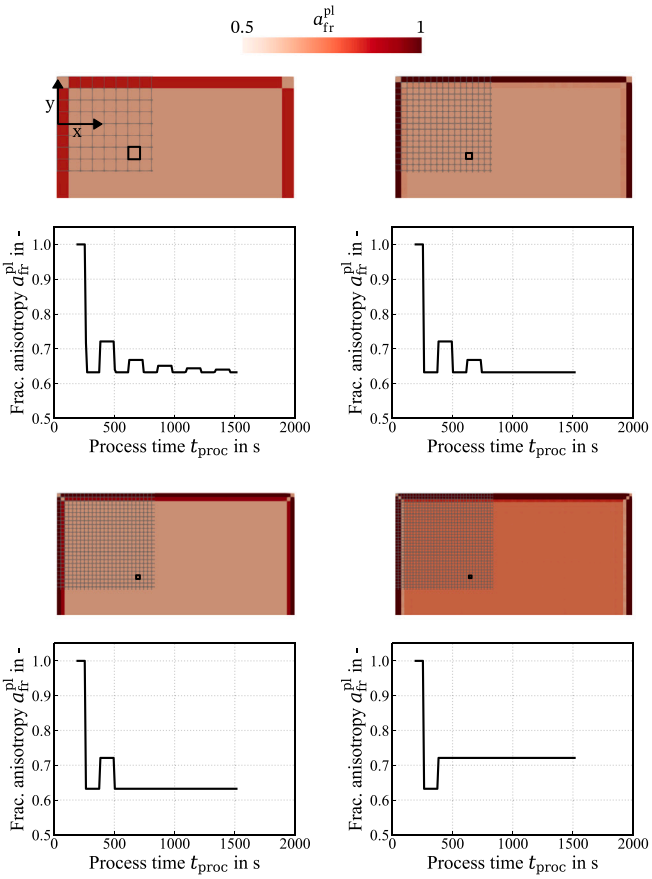

Fig. 8. Influence of element size on the evolution of material orientation over time for the infill mesostructure. Element sizes 2.4 mm, 1.2 mm, 0.8 mm and 0.6 mm are shown in this order from top left to bottom right. The strand width was 0.4 mm and the height was 0.2 mm.

and turning points) using the built-in method in *Abaqus*, the element height would have to correspond to the layer height, which would drastically increase the number of elements and computation time. The presented method therefore offers a practical advantage by accurately representing evolving anisotropy even with coarser meshes and, more generally, represents an advancement beyond the state of the art in computational modeling of material orientation in MEX.

Fig. 8 shows the influence of the element size on the change in material orientation over time for the infill mesostructure. The element size affects the local stiffness evolution during the process, as it determines how many layers are combined within a single element. The study further reveals that the number of layers per element, specifically whether it is even or odd, has a significant impact on the resulting orientation distribution. When the element height is an even multiple of the layer height and alternating infill patterns are used, each element in the infill region tends to receive the same orientation. In contrast, for odd multiples, alternating orientations are retained within the element layers. This leads to a stepwise variation in stiffness between adjacent elements, which can in turn cause convergence issues in the simulation. Additionally, the variation in resulting orientation decreases with increasing element size. When the infill pattern remains constant across all layers, the resulting orientation per element is unaffected by the element height.

The investigations in this section show that the presented methodology can generally be used to represent local changes in the mesostructure, such as the mesostructure categories introduced in Section 2.1. A smaller element size allows a finer resolution of the different structures,

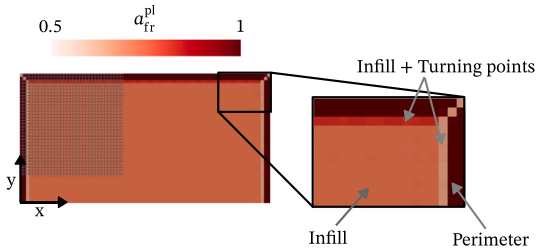

Fig. 9. Illustration of local mesostructure changes for an element edge length of 0.6 mm.

however, an even number of layers per element is recommended to avoid stiffness jumps. This is illustrated again in Fig. 9 for the element edge length of 0.6 mm. It can be seen that the element size and the associated uneven number of layers in the element result in different orientation states in the "Perimeter + Infill + Turning points" region.

2.3. Equivalent isotropic approach

To obtain a representative equivalent isotropic description of an orthotropic stiffness tensor $\mathbb{C}_{ortho}$ (representative of the material and its microstructure), the equivalent isotropic stiffness tensor $\bar{\mathbb{C}}_{iso}$ can be calculated by integrating over all possible rotations $\boldsymbol{Q}$ in the special orthogonal group $\mathcal{SO}(3)$:

$$\bar{\mathbb{C}}_{iso} = \int_{\mathcal{SO}(3)} \boldsymbol{Q} \star \mathbb{C}_{ortho}, \mathrm{d}\boldsymbol{Q}. \tag{18}$$

Using the isotropic projection operators $\mathbb{P}1$ and $\mathbb{P}2$, this expression can be algebraically transformed as follows:

$$\bar{\mathbb{C}}_{iso} = \int_{\mathcal{SO}(3)} \boldsymbol{Q} \star \mathbb{C}_{ortho}, \mathrm{d}\boldsymbol{Q} = \left(\mathbb{C}_{ortho} \cdot \mathbb{P}_1\right) \frac{\mathbb{P}_1}{|\mathbb{P}_1|^2} + \left(\mathbb{C}_{ortho} \cdot \mathbb{P}_2\right) \frac{\mathbb{P}_2}{|\mathbb{P}_2|^2} \tag{19}$$

with $\mathbb{P}_1 = 1/3(\boldsymbol{I} \otimes \boldsymbol{I})$ and $\mathbb{P}_2 = \mathbb{I}^S - \mathbb{P}_1$, where $\mathbb{I}^S$ denotes the identity on symmetric second-order tensors. This formulation is derived from the orthogonal decomposition of $\mathbb{C}_{ortho}$ into its isotropic components. The projection coefficients are obtained by contraction with $\mathbb{P}_1$ and $\mathbb{P}_2$, ensuring that only the isotropic contributions are retained. The normalization by $|\mathbb{P}_i|^2$ guarantees the correct scaling of the projected components.

3. Experimental validation

In the experimental validation, the proposed approach is additionally compared with an isotropic stiffness description, as commonly used in literature. The equivalent isotropic approach used here was presented in Section 2.3. A comparison with the *Abaqus* fixed-orientation approach is not included, since for the 0° and 90° infill cases, used here as boundary cases, both anisotropic models yield nearly identical stiffness tensors, apart from minor perimeter and turning-point effects, which are captured by the proposed approach presented in this work. The advantage of the proposed approach over the *Abaqus* build-in approach has already been discussed in Section 2.2.3 for alternating infill angles on coarse meshes.

3.1. Material

The exemplary material used for validation is the commercial Ultrafuse polylactic acid (PLA) filament from Forward AM with a processing temperature of $T_{proc} = 210\,°C - 230\,°C$ according to the supplier [42].

Table 1
Engineering constants for the orthotropic stiffness tensor $\mathbb{C}^{\text{exp}}_{\text{ortho}}$.

E_{11} (MPa)	E_{22} (MPa)	E_{33} (MPa)	ν_{12} –	ν_{13} –	ν_{23} –	G_{12} (MPa)	G_{13} (MPa)	G_{23} (MPa)
3257	2469	2667	0.35	0.27	0.31 [45]	953	1029	803

3.1.1. Material characterization

The density is $1208\,\text{kg}\,\text{m}^{-3}$ according to [43]. The temperature-dependent specific heat capacity $c_p(T)$ was also taken from [43]. The thermal conductivity was assumed to be constant and isotropic, with a value of $\kappa = 0.17\,\text{W/m K}$, based on the average values reported in [44].

The material parameters for the typical orthotropic behavior of the material resulting from the process are listed in Table 1. The material constants were primarily determined through uniaxial tensile tests conducted at various orientations. These tests were performed on specimens composed of multiple layers, ensuring that effective properties of the mesostructure inherently account for interlayer and intralayer effects influencing the deformation behavior. The elastic moduli (E_{11}, E_{22}, E_{33}) and Poisson's ratios (ν_{12}, ν_{13}) were determined directly by experiment. Then, the shear moduli G_{ij} were calculated using classical laminate theory (CLT), as recommended by Tröger et al. [45], which is based on the assumption of a laminate-like structure. The shear moduli G_{ij} are determined by the following equation:

$$G_{ij} = \left(\frac{4}{\hat{E}^{xx}_{ij}} - \frac{1}{E_{ii}} - \frac{1}{E_{jj}} + \frac{2\nu_{ij}}{E_{ii}} \right)^{-1}, \tag{20}$$

where $\hat{E}^{xx}_{ij}$ describes the Young's modulus of tensile specimens rotated 45° in the i-j plane.

Due to experimental limitations, values from the literature $(\cdot)^{\text{Tr}}$ [45] were used for parameters that could not be determined directly (in particular, ν_{23}, $\hat{E}^{xx}_{13}$, and $\hat{E}^{xx}_{23}$). These values were adjusted to align with our measurements using the following scaling:

$$\nu_{23} = \nu^{\text{Tr}}_{23}, \quad \hat{E}^{\text{xx}}_{13} = \hat{E}^{\text{xx}}_{12} \frac{\hat{E}^{\text{xx,Tr}}_{13}}{\hat{E}^{\text{xx,Tr}}_{12}}, \quad \hat{E}^{\text{xx}}_{23} = \hat{E}^{\text{xx}}_{12} \frac{\hat{E}^{\text{xx,Tr}}_{23}}{\hat{E}^{\text{xx,Tr}}_{12}} \tag{21}$$

In this way, the orthotropic stiffness tensor $\mathbb{C}^{\text{exp}}_{\text{ortho}}$ of the investigated MEX mesostructure could be determined based on experimental results and validated literature data (see Table 1).

In order to minimize manufacturing influences, such as those from the perimeter or inflection points of the deposited polymer strands, our previous investigations were referenced to ensure accurate characterization of the mechanical properties [46]. The specimens were cut from an additively manufactured plate following the specifications outlined in [46].

Dynamic mechanical analysis (DMA) experiments were conducted to evaluate the temperature dependence of stiffness. Fig. 11(a) shows, in gray, the measured storage modulus E' in the extrusion direction (0° infill angle) previously published by Frölich et al. [47]. The increase around 75 °C is attributed to cold crystallization effects. As the tests were conducted on printed specimens, the material was amorphous, which is confirmed by additional experimental investigations presented in [47]. The resulting amorphous modeling of the process leads to the assumed curve of E' in black in Fig. 10(a), without the increase due to cold crystallization. A further decrease in stiffness for temperatures above 75 °C has been neglected here.

To determine the coefficient of thermal expansion (CTE) α_{th}, thermomechanical analysis (TMA) was performed on printed specimens. The experimental procedure and results are published in [47], showing that a temperature-dependent, isotropic description is permissible. The measured length change is shown in gray in Fig. 10(b), with the simulation assuming a smoothed curve, represented in black in the figure.

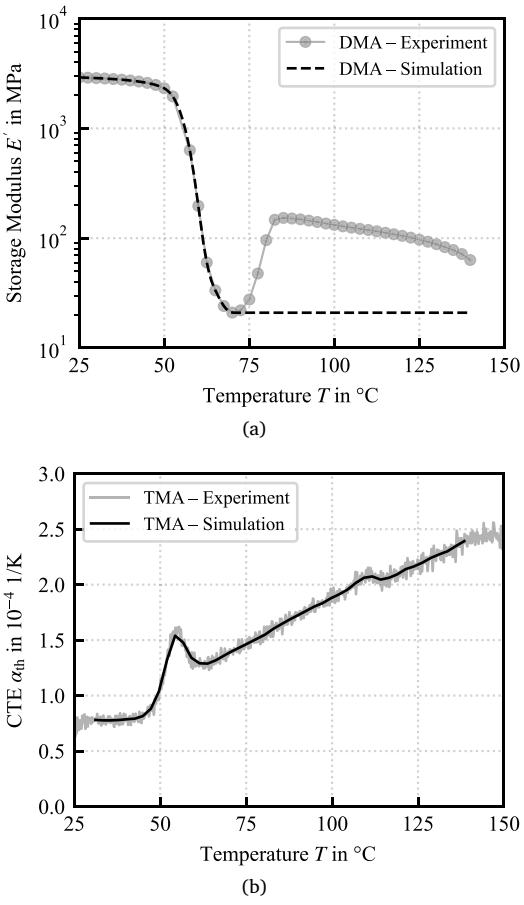

Fig. 10. (a) Storage modulus E' as a function of temperature obtained from DMA measurements on unidirectionally printed specimens with extrusion direction aligned with the load. The assumed curve for simulation includes the softening range, but no cold crystallization as the PLA remains amorphous during printing. (b) Thermal expansion behavior from TMA measurements on printed specimens, along with the assumed curve used to determine the coefficient of thermal expansion (CTE) α_{th} used in simulation. Experimental data were published in previous work [47].

3.1.2. Material modeling

In the thermal simulation, an isotropic and temperature-independent heat transfer coefficient and a isotropic as well as temperature-dependent specific heat capacity are set as described in Section 3.1.1.

In the mechanical simulation a path-dependent material model is used to consider the viscoelastic behavior [48]. The viscoelastic behavior is modeled in a simplified way by assuming that the relaxation time τ below a certain vitrification temperature T_{vitr} tends toward infinity (glassy state) and above this temperature tends toward 0 (rubbery state). According to the path-dependent material model, the resulting Cauchy stress $\boldsymbol{\sigma}$ can be additively decomposed into an elastic part ($\boldsymbol{\sigma}_{\text{el}}$) and a simplified pseudo-viscoelastic part ($\boldsymbol{\sigma}_{\text{ve}}$):

$$\boldsymbol{\sigma} = \boldsymbol{\sigma}_{\text{el}} + \boldsymbol{\sigma}_{\text{ve}}. \tag{22}$$

The elastic part $\boldsymbol{\sigma}_{\text{el}}$ in the current time increment t_i is described by

$$\boldsymbol{\sigma}_{\text{el}}(t_i) \approx \boldsymbol{\sigma}_{\text{el}}(t_{i-1}) + \mathbb{C}_{\infty}(\Delta\boldsymbol{\varepsilon}(t_i) - \Delta\boldsymbol{\varepsilon}_{\text{th}}(t_i)). \tag{23}$$

with $\boldsymbol{\sigma}_{\text{el}}$ in the preceding time increment t_{i-1}, the stiffness $\mathbb{C}_{\infty}$ above T_{vitr}, the strain increment $\Delta\boldsymbol{\varepsilon}$, and the thermal strain increment $\Delta\boldsymbol{\varepsilon}_{\text{th}}$.

$\Delta\varepsilon_{th}$ is described by

$$\Delta\varepsilon_{th}(t_i) = \alpha_{th}(T(t_i) - T(t_{i-1})). \tag{24}$$

The viscoelastic part σ_{ve} of the Cauchy stress is simplified by the two limit cases:

$$\sigma_{ve}(t_i) = \begin{cases} \mathbf{0}, & T \geq T_{vitr} \\ \sigma_{ve}(t_{i-1}) + \Delta\mathbb{C}[\Delta\varepsilon(t_i) - \Delta\varepsilon_{th}(t_i)], & T < T_{vitr}. \end{cases} \tag{25}$$

Above T_{vitr}, σ_{ve} is $\mathbf{0}$, since the relaxation time tends to 0. Below T_{vitr}, σ_{ve} is calculated from σ_{ve} from the previous time increment, the softening of the stiffness $\Delta\mathbb{C}$ at T_{vitr}, $\Delta\varepsilon$ and $\Delta\varepsilon_{th}$. The viscoelastic behavior is thus simplified by a purely elastic response in two successive, independent steps (in contrast to the Chile model). This is important because the material can exceed and fall below T_{vitr} several times and the relaxation of the built-up stresses is taken into account when reheating.

The softening of the stiffness $\Delta\mathbb{C}$ is described with the relative softening coefficient a as follows:

$$\Delta\mathbb{C} = \mathbb{C}_0 - \mathbb{C}_\infty = a\mathbb{C}_0. \tag{26}$$

Here, $\mathbb{C}_0$ is the local stiffness tensor below T_{vitr}.

In this research, T_{vitr} is defined as the midpoint of the softening range. The corresponding softening range is illustrated in Fig. 10(a). Since there is no uniform definition of the softening range of thermoplastic materials based on DMA measurements, this study used a consistent and practical criterion. The upper limit of the softening range is the temperature at which the storage modulus transitions to a plateau ($dE'/d = 0$) and reaches its minimum. This reflects the complete softening of the material. The lower limit of the softening range is defined as the temperature at which E' decreases by 20% of the maximum dE'/d change. This procedure provides a reproducible, transparent definition of mechanical softening behavior based on the E' curve characteristics. Therefore, using this approach, T_{vitr} is determined to be 59.23 °C.

The DMA measurements were also used to determine the relative softening coefficient a: The coefficient $a = 0.991$ was calculated using

$$a = 1 - \left(\frac{\min(E')}{\max(E')}\right). \tag{27}$$

The effective stiffness tensors $\bar{\mathbb{C}}_0$ used in the simulations are derived from the experimentally determined orthotropic stiffness tensor in Table 1, following the anisotropic and equivalent isotropic homogenization approaches introduced in Section 2. The anisotropic model uses a locally varying $\bar{\mathbb{C}}_0$ that evolves with the element-wise orientation tensors over time according to the explanations in Section 2.2. In contrast, the equivalent isotropic model employs a spatially and temporally constant stiffness tensor, obtained by projecting the orthotropic tensor onto the isotropic subspace via Eq. (19). The resulting directional strain energy densities $W(\boldsymbol{n})$ of the equivalent isotropic stiffness tensor, compared to those derived from the experimentally determined orthotropic tensor, are shown in Fig. 11. The thermomechanical model is implemented via a *UMAT* subroutine.

Table 2
Slicer and process parameters selected.

Process parameter	Value	Unit
Nozzle temperature T_N	220	°C
Bed temperature T_{bed}	40	°C
Layer height l_{height}	0.2	mm
Extrusion width e_{width}	0.4	mm
Infill density	100	%
Print speed v_{print}	50	mm s^{-1}

3.2. Component design

For the validation, a component geometry was chosen that leads to an expected PiD and allows for a simple evaluation. The geometry is shown in Fig. 12. The trapezoidal cross-section, leads to residual stresses that cause the component to bend around the y-axis when removed from the build plate. This bending is the direct measure of the PiD.

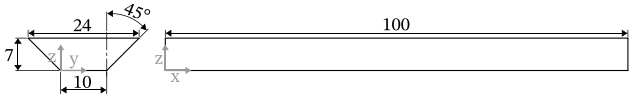

Fig. 12. Geometry and dimensions of the validation component in mm.

3.3. Experimental tests

3.3.1. MEX process design

The Ultimaker 2+ from Ultimaker was used to produce the components in this work. The Ultimaker has a heated printing bed. The standard glass printing bed has been replaced with an unused FilaPrint permanent printing bed to ensure the most reproducible adhesion possible. The nozzle has a diameter of 0.4 mm and a print resolution of 200 µm. The print bed was leveled with three adjustment screws. The slicer and printer settings listed in Table 2 were selected based on printing studies to achieve a consistent and reproducible mesostructure. To investigate the influence of the trajectory on the PiD, an infill with orientation of 0° or 90° to the x-axis was selected. The components with the selected fill orientation are shown in Fig. 13. For each configuration, three components were printed and measured.

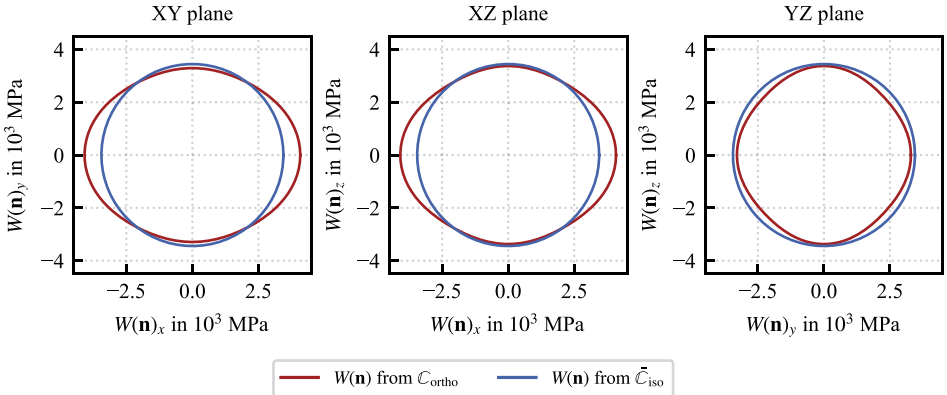

Fig. 11. Directional strain energy density response derived from orthotropic and equivalent isotropic stiffness tensors. The plots show $W(\boldsymbol{n}) = \frac{1}{2}(\boldsymbol{n}\otimes\boldsymbol{n}) : \mathbb{C} : (\boldsymbol{n}\otimes\boldsymbol{n})$ evaluated for all in-plane directions $\boldsymbol{n}$ in the XY, XZ, and YZ planes. Units are given in MPa, corresponding to elastic strain energy density under unit strain in direction $\boldsymbol{n}$.

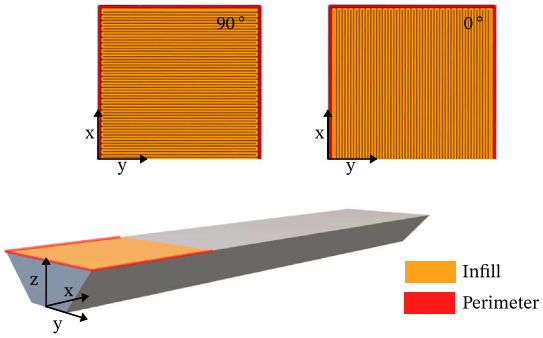

Fig. 13. Cross section of the trajectory of the validation components with infill of 100% with 0° and 90° orientations to the x-axis in orange and one perimeter in red.

3.3.2. X-ray computed tomography (μCT)

The validation components were scanned using a YXLON CT precision μCT system from Yxlon International CT GmbH in Hattingen, Germany. This system features a µm-focused X-ray reflection tube with a tungsten target and a high-resolution PerkinElmer Y.XRD1620 flat image detector with 2048 pixels × 2048 pixels. The scan parameters are listed in Table B.3 in the Appendix. The contour of each specimen was determined from the corresponding scans and exported as an STL file.

3.3.3. Experimental results

The measured curvature of the underside of the component was evaluated using an in-house *Python* tool. Within this tool, the scanned 3D surface model in STL format is loaded to analyze the deformation along a defined path on the component (red path in Fig. 14(a)). An equidistant point path is generated between a start and end point in space, and the points are then projected onto the nearest points on the component surface using a k-d tree for nearest neighbor search (*cKDTree*). The projected path points obtained in this way form the basis for the quantitative evaluation of the local deformations along the path under consideration.

The results, shown in Fig. 14(b), include measurements at both 0° and 90° infill angles. The mean of the three measurements and their scatter are presented, revealing a reproducible PiD. A significant influence of the selected trajectory, shown in Fig. 13, on the PiD can bee seen: At 90° infill angle, a lower PiD occurs compared to the 0° infill angle.

3.4. Process simulation

In the FE process simulation, the entire process chain up to the final component is modeled using the AM-Modeler in *Abaqus* [15]:

(1) Print the component with a sequentially coupled thermomechanical simulation.
(2) Cool the component by a predefined cooling curve of the printing plate.
(3) Detach the component from the printing plate.

Fig. 15 shows the individual steps of the process simulation chain.

To model the printing process, a cube with the maximum dimensions of the validation component in the global coordinate system is created and discretized with hexahedral elements as a starting point (initial step in Fig. 15). Trilinear hexahedral elements are used for thermal simulations, while tri-quadratic hexahedral elements with reduced integration are employed for thermomechanical simulations. Based on a sensitivity analysis, a compromise is chosen between the accuracy of the component PiD prediction and computational efficiency. A time

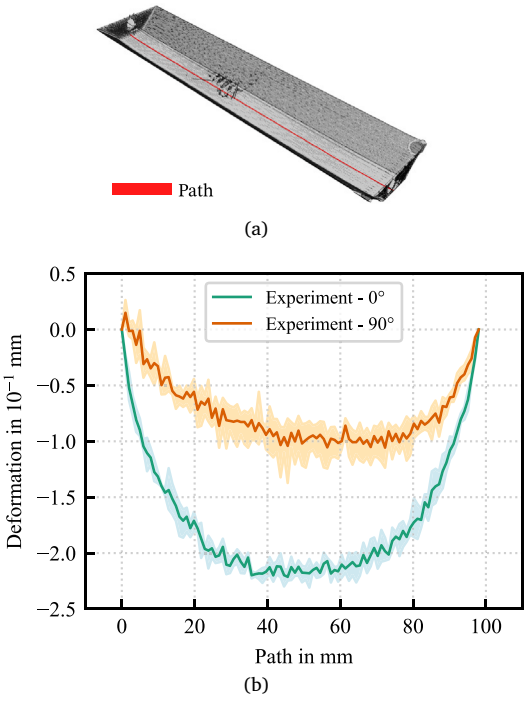

Fig. 14. (a) Validation component measured using μCT, with the evaluation path highlighted in red. (b) Mean curvature (solid line) and minimum/maximum range (shaded envelope) of the underside of the component for specimens printed with 0° (green) and 90° (orange) infill angle.

increment of $t_{inc} = 5$ s and element edge lengths of 1 mm × 1 mm × 0.4 mm are specified. Further details on the sensitivity analysis with regard to t_{inc} are provided in the Appendix C. It should be noted that no dedicated mesh convergence study was conducted because a finer mesh would result in unreasonably long computation times. However, a relatively fine mesh with an element height twice the layer height was used. In this context, it is also important to note that the presented methodology was specifically developed for cases requiring coarse meshes. Nevertheless, a finer mesh would provide a more realistic representation of the process, including the temperature distribution, which could affect the predicted deformations.

The elements are activated according to the specified event series, ensuring that only the actual printed material are activated. To consider hardware limitations, the event series is decoded from the G-Code using the *Python* tool *pyGCodeDecode* [39,40]. The initial temperature of the elements is set to the extrusion temperature of 220 °C. In the thermal simulation, the temperature of the printing plate is specified as a Dirichlet boundary condition at the nodes located at the bottom of the activated component. The build plate temperature is set to 40 °C throughout the printing and cooling steps, consistent with the experimental setup. Heat loss to the environment was modeled through both convection and radiation. The convection coefficient is set to $h_{conv} = 8\,\mathrm{W/m^2\,K}$ and the emissivity coefficient is set to $\epsilon = 0.97$ according to [49].

During the subsequent thermomechanical simulation, the component is fixed to the build plate via a Dirichlet boundary condition applied to these nodes. This condition remains until the component is detached from the plate, at which point the Dirichlet boundary condition is deactivated. The detachment from the build plate is modeled as an instantaneous release by deactivating the boundary condition at the corresponding nodes in a single simulation step. To ensure static determinacy, the boundary conditions are selected according to the procedure outlined in [24].

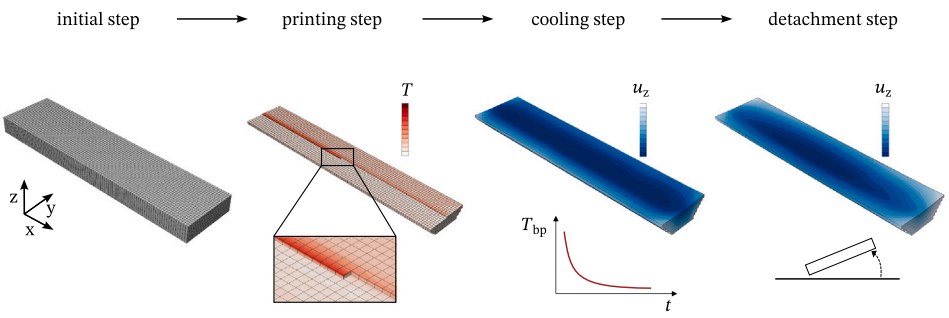

Fig. 15. Individual steps in the MEX process chain during process simulation to predict PiD. In the "initial Step", domains containing inactive elements are created. In the "printing Step", the MEX process is mapped using a sequentially coupled simulation with a fixed build plate temperature T_{bp} of 40 °C. The T_{bp} is then approximated to room temperature over a certain period of time in the "cooling Step". Finally, in the "detach Step", the component is detached from the build plate.

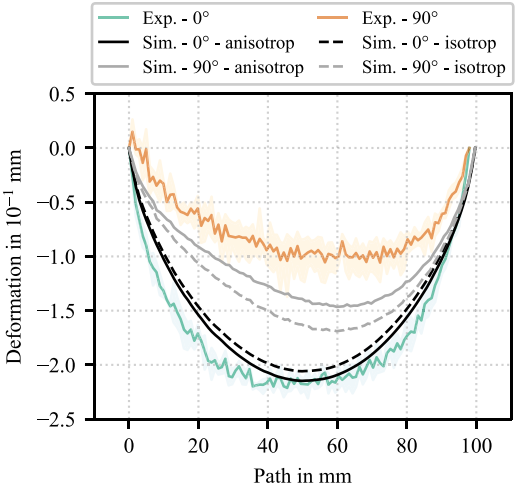

Fig. 16. Comparison of experimentally determined and numerically predicted deformation in green using the presented anisotropic and equivalent isotropic approaches.

3.5. Validation results

Fig. 16 shows the experimentally determined and numerically predicted PiD for infill angles of 0° and 90°, calculated using both the anisotropic (solid line) and equivalent isotropic (dashed line) approaches. For both infill orientations, the qualitative progression of the deformation is captured accurately, with a considerably larger PiD observed for 0° than for 90°. The anisotropic approach achieves good quantitative agreement, particularly at 0°. For 90°, the PiD is slightly overestimated. The prediction inaccuracy, especially for 90° infill, is primarily due to the selected material model, which significantly simplifies the relaxation processes. Note that the maximum deformation is also influenced by the selected T_{vitr}.

Compared to the anisotropic model, the equivalent isotropic approach underpredicts the deformation at 0° by approximately 4% and overpredicts it at 90° by about 16%. This highlights the importance of incorporating orientation-dependent mechanical properties into the simulation. The differences between the two approaches can be explained as follows: The deformation observed in the equivalent isotropic model arises from variations in the timing and spatial distribution of material deposition. These differences lead to distinct thermal histories and, consequently, to infill-dependent deformation, even when mechanical anisotropy is not considered. The anisotropic model additionally accounts for the orientation-dependent stiffness introduced by the deposition path.

For an infill angle of 0°, the strands are aligned along the x-direction, resulting in increased stiffness in that direction. This increased stiffness is explicitly captured in the anisotropic model, whereas it is averaged out in the equivalent isotropic model. As a result, thermal expansion leads to higher residual stresses in the anisotropic model during cooling, which in turn cause larger deformations. In contrast, for a 90° infill, the equivalent isotropic model overestimates the stiffness in the x-direction, leading to an overprediction of deformation.

These findings highlight the importance of incorporating deposition-induced material anisotropy when aiming to reliably predict process-induced deformation, especially in materials with high thermal expansion coefficients or pronounced direction-dependent behavior.

4. Conclusion

This work presents a homogenization approach for predicting trajectory-dependent process-induced deformation (PiD) in material extrusion (MEX) using finite element (FE) simulations. The method addresses the challenge of integrating process-specific mesostructures into component-scale simulations without requiring explicit resolution at the layer or strand level, thus maintaining computational efficiency.

The key contributions of this study can be summarized as follows:

- The method builds upon the orientation averaging framework by Advani and Tucker, extended to capture the orthotropic nature of MEX mesostructures. Second- and fourth-order orientation tensors model in-plane strand orientation variations, enabling accurate local anisotropic stiffness calculation during printing.
- The print trajectory, specified in the G-Code, is mapped to spatial orientation fields via an efficient k-nearest neighbor search. This assigns anisotropic stiffness properties to the finite elements.
- The approach is verified with numerical benchmarks. Furthermore, numerical studies showing that orientation states evolve within elements and that complex mesostructural features (e.g., perimeters, turning points, mixed orientations) can be captured without fine layer- or strand-level discretization.
- Experimental validation is carried out using PLA specimens characterized via X-ray computed tomography. The predicted PiD showed good quantitative agreement for 0° infill and a slight overestimation for 90°, while the overall deformation behavior was captured qualitatively well in all cases.
- Comparison with an equivalent isotropic stiffness approach demonstrates the superior capability of the anisotropic approach to reflect trajectory-dependent effects on deformation.

Based on the results, the key findings of this study are:

- The local mesostructure evolves dynamically during printing, resulting in spatially and temporally varying orientation states within individual finite elements. Numerical studies for a 0/90° infill pattern highlight the importance of continuously updating orientation tensors, rather than assuming fixed or isotropic orientations.
- The anisotropic modeling approach demonstrates that PiD depends not only on local strand deposition and temperature distribution, but also significantly on the spatial variation of effective stiffness.
- By relying on orientation states derived solely from printing trajectory data and computing effective stiffness tensors from any chosen orthotropic material model, the presented method is fundamentally material-independent and represents an advancement beyond state-of-the-art approaches relying on isotropic assumptions or fixed initial orientations (e.g., *AM Modeler* in *Abaqus*). This flexibility allows broad applicability across different polymers and material behaviors.

The proposed method offers a scalable solution for accurately predicting PiD in MEX processes and provides valuable insights into the impact of inhomogeneous, trajectory-dependent stiffness distributions on deformation during printing. This enables more efficient and resource-conscious processing of deformation-prone materials. Furthermore, the method achieves this accuracy without requiring layer-level discretization, allowing for significant computational savings compared to fixed-orientation approaches.

In addition, the method offers clear benefits for subsequent structural simulations, where capturing the final, spatially varying stiffness distribution is essential for reliably predicting component performance under real-world loading conditions.

Future work could focus on coupling the presented framework with microstructure-informed material models of discontinuous fiber reinforces polymers to further enhance its predictive capabilities and to establish a more direct link between microstructural formation and the resulting anisotropic material behavior.

CRediT authorship contribution statement

Felix Frölich: Writing – original draft, Visualization, Validation, Software, Methodology, Investigation, Formal analysis, Data curation, Conceptualization. **Mario Emanuele Di Nardo:** Writing – review & editing, Software, Methodology. **Constantin Krauß:** Writing – review & editing, Methodology. **Anselm Heuer:** Writing – review & editing, Validation, Investigation. **Wilfried V. Liebig:** Writing – review & editing, Supervision. **Florian Wittemann:** Writing – review & editing, Supervision, Methodology. **Pierpaolo Carlone:** Writing – review & editing, Supervision. **Luise Kärger:** Writing – review & editing, Supervision, Funding acquisition, Conceptualization.

Declaration of Generative AI and AI-assisted technologies in the writing process

During the preparation of this work the authors used *Deepl* in order to improve language and readability. After using this tool, the authors reviewed and edited the content as needed and take full responsibility for the content of the publication.

Declaration of competing interest

The authors declare that they have no known competing financial interests or personal relationships that could have appeared to influence the work reported in this paper.

Table B.3
Scan parameters for μCT scans of the validation components.

Scan parameter	Value	Unit
Voltage	140	kV
Current	0.25	mA
Voxel size	65.84	µm
Line binning parameter	2	–
Number of projections	3000	ms
Exposure/Integration time	1000	ms

Acknowledgments

The authors thank Baden-Württemberg Ministry of Science, Research and Arts (MWK) for funding the subsequent project underlying this work, "Basics of a remanufacturing process chain for functional, hybridized polymer components to increase reusability and optimize resource utilization (Restore)" as part of the Innovation-Campus Future Mobility (ICM), and the German Research Foundation (DFG) for funding Prof. Kärger's Heisenberg Professorship (project no. 455807141).

Appendix A. Note on out-of-plane orientations and sparse structures

This work is based on the planar (x–y) deposition that is typical of MEX processes. However, the orientation tensor formulation presented here can be extended to three-dimensional (3D) deposition paths by including a non-zero z-component in the orientation vector, $\boldsymbol{p}$. The tensor formulation remains valid in this case.

However, to convert the material orientation into a stiffness formulation for 3D additive manufacturing, the orientation averaging would need to be revised. This is because the presented approach exploits the fact that the third orthotropic material axis, $\boldsymbol{e}_3$, is always aligned with the global build direction.

Furthermore, since the method requires complete filling, stiffness predictions for sparse or lattice-like structures must consider the local material volume fraction.

Appendix B. Scan parameters for μCT scans

See Table B.3.

Appendix C. Sensitivity studies for t_{inc}

To evaluate the effect of the time increment t_{inc} on the resulting component deformation, the increment was varied as shown in Fig. C.17. Fig. C.17(a) shows the temperature curve over the entire process chain. The initial temperature of 220 °C is followed by the period during which the material is heated and cooled during the process. After the printing process (after about 3200 s), the cooling on the printing plate follows. The time increment mainly affects the temperature curve during printing immediately after the elements are activated. Fig. C.17(b) illustrates this range. Here it can be seen that the time increment influences the maximum temperature during reheating: the smaller the increment, the higher the temperature reached. As the increment increases, the process-typical temperature curve is no longer accurately represented. From a certain increment (here $t_{\mathrm{inc}} = 100$ s) the typical temperature peaks no longer occur.

The thermomechanical simulation based on the corresponding thermal simulation results in the deformations shown in Fig. C.18. The curved progression of the PiD is predicted with all selected t_{inc}, but the predicted PiD is overestimated for larger t_{inc} Fig. C.19 provides an overview of the influence of time increment size on the computational effort and on the deformation results to enable an efficient numerical prediction. All simulations were conducted on the same workstation

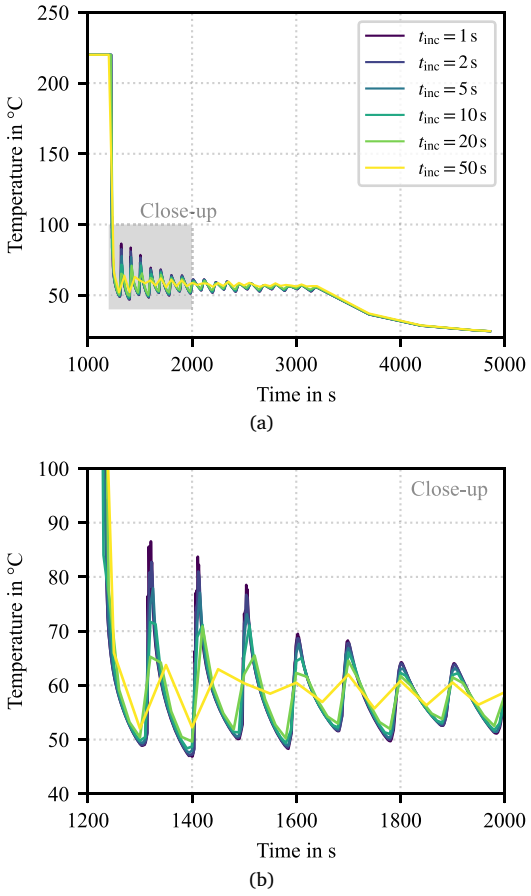

Fig. C.17. Temperature profiles over time in the center of the component for different time increments.

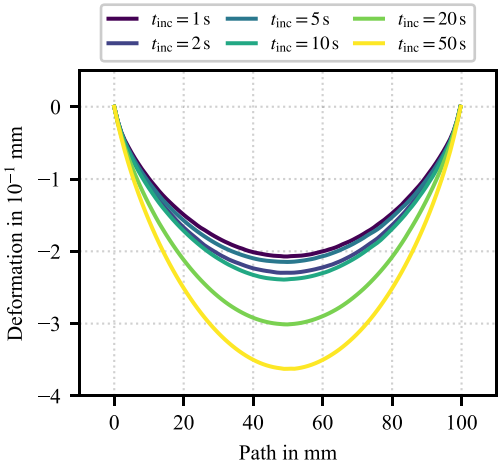

Fig. C.18. Simulation-based determination of component deflection in the z-direction for different time increments.

equipped with an AMD Ryzen Threadripper PRO 3975WX CPU @ 3.50 GHz and 32 GB of RAM. Each simulation was executed using 4 CPU cores. This setup ensures consistent computational performance across all cases. Fig. C.19(a) shows the total computation time required for each discretization as a function of the time increment. Fig. C.19(b) shows the maximum deformation versus the time increment, with the data points color-coded according to the required computation time. The predicted maximum PiD generally decreases with a smaller time

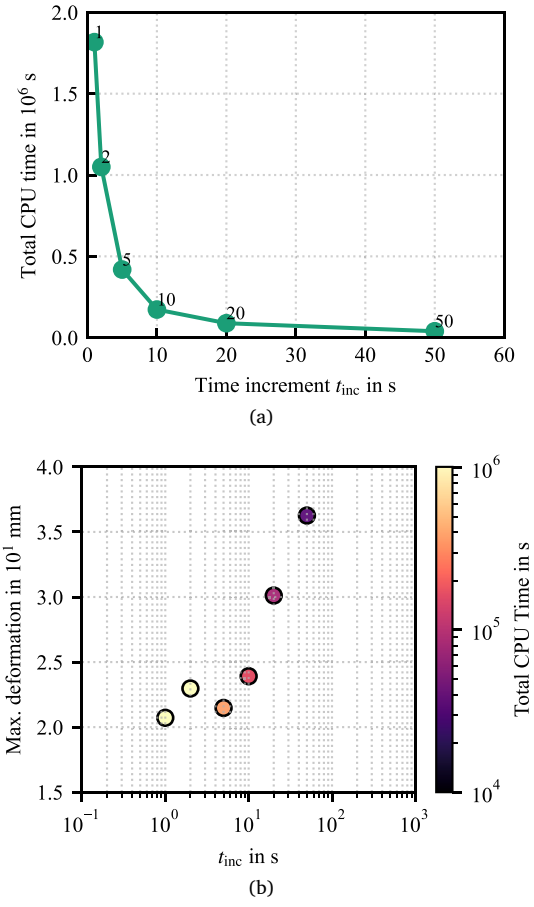

Fig. C.19. (a) Required total computation time for each discretization, plotted as a function of time increment. (b) Maximum predicted deformation for different time increments. The required computation time is color-coded.

increment. This trend continues down to $t_{inc} = 5\,s$, below which the results begin to fluctuate. This fluctuation indicates that no clear systematic improvement in prediction accuracy can be expected below this value. In particular, transient thermomechanical effects occurring at sub-5-second scales did not significantly alter the predicted deformation behavior in this model. At the same time, the computational cost rises significantly for smaller increments. For example, the simulation with a $t_{inc} = 1\,s$ required a total CPU time of 500 h. To compare with experimentally measured deformations, a simulation with a time increment of $t_{inc} = 5\,s$ was selected as a compromise between numerical accuracy and computational efficiency.

Data availability

Data will be made available on request.

References

[1] H. Klippstein, A. Diaz De Cerio Sanchez, H. Hassanin, Y. Zweiri, L. Seneviratne, Fused deposition modeling for Unmanned Aerial Vehicles (UAVs): A review, Adv. Eng. Mater. 20 (2) (2018) 1700552, http://dx.doi.org/10.1002/adem.201700552.

[2] L.G. Blok, M.L. Longana, H. Yu, B.K. Woods, An investigation into 3D printing of fibre reinforced thermoplastic composites, Addit. Manuf. 22 (March) (2018) 176–186, http://dx.doi.org/10.1016/j.addma.2018.04.039.

[3] J.P. Lewicki, J.N. Rodriguez, C. Zhu, M.A. Worsley, A.S. Wu, Y. Kanarska, J.D. Horn, E.B. Duoss, J.M. Ortega, W. Elmer, R. Hensleigh, R.A. Fellini, M.J. King, 3D-Printing of meso-structurally ordered carbon fiber/polymer composites

with unprecedented orthotropic physical properties, Sci. Rep. 7 (2017) 1–14, http://dx.doi.org/10.1038/srep43401.
[4] P. Parandoush, D. Lin, A review on additive manufacturing of polymer-fiber composites, Compos. Struct. 182 (2017) 36–53, http://dx.doi.org/10.1016/j.compstruct.2017.08.088.
[5] J. Kiendl, C. Gao, Controlling toughness and strength of FDM 3D-printed PLA components through the raster layup, Compos. B 180 (2020) 107562, http://dx.doi.org/10.1016/j.compositesb.2019.107562.
[6] H.L. Tekinalp, V. Kunc, G.M. Velez-Garcia, C.E. Duty, L.J. Love, A.K. Naskar, C.A. Blue, S. Ozcan, Highly oriented carbon fiber–polymer composites via additive manufacturing, Compos. Sci. Technol. 105 (2014) 144–150, http://dx.doi.org/10.1016/j.compscitech.2014.10.009.
[7] M. Coca-Gonzalez, M. Jimenez-Martinez, Warpage: Causes, manufacturing processes and future challenges: A review, Proc. Inst. Mech. Eng. L: J. Mater.: Des. Appl. 239 (6) (2025) 1201–1217, http://dx.doi.org/10.1177/14644207241285399.
[8] M. Moretti, N. Senin, In-process monitoring of part warpage in fused filament fabrication through the analysis of the repulsive force acting on the extruder, Addit. Manuf. 49 (2022) 102505, http://dx.doi.org/10.1016/j.addma.2021.102505.
[9] E.R. Fitzharris, N. Watanabe, D.W. Rosen, M.L. Shofner, Effects of material properties on warpage in fused deposition modeling parts, Int. J. Adv. Manuf. Technol. 95 (5) (2018) 2059–2070, http://dx.doi.org/10.1007/s00170-017-1340-8.
[10] A. Yadav, P. Rohru, A. Babbar, R. Kumar, N. Ranjan, J.S. Chohan, R. Kumar, M. Gupta, Fused filament fabrication: A state-of-the-art review of the technology, materials, properties and defects, Int. J. Interact. Des. Manuf. (IJIDeM) 17 (6) (2023) 2867–2889, http://dx.doi.org/10.1007/s12008-022-01026-5.
[11] Y. Zhang, Y. Chou, Three-dimensional finite element analysis simulations of the fused deposition modelling process, Proc. Inst. Mech. Eng. B 220 (10) (2006) 1663–1671, http://dx.doi.org/10.1243/09544054JEM572.
[12] Y. Zhang, K. Chou, A parametric study of part distortions in fused deposition modelling using three-dimensional finite element analysis, Proc. Inst. Mech. Eng. B 222 (8) (2008) 959–967, http://dx.doi.org/10.1243/09544054JEM990.
[13] A.J. Favaloro, E. Barocio, B. Brenken, R.B. Pipes, E. Barocio, R.B. Pipes, Simulation of polymeric composites additive manufacturing using abaqus, in: Dassault Systémes' Science in the Age of Experience, Chicago, IL, 2017.
[14] B. Brenken, E. Barocio, A. Favaloro, V. Kunc, R.B. Pipes, Development and validation of extrusion deposition additive manufacturing process simulations, Addit. Manuf. 25 (2019) 218–226, http://dx.doi.org/10.1016/j.addma.2018.10.041.
[15] Dassault Systémes Simulia Corp., SIMULIA user assistance - about additive manufacturing process simulation, 2024, URL https://help.3ds.com/2024/english/DSSIMULIA_Established/SIMACAEANLRefMap/simaanl-c-amabout.htm?contextscope=all, Version 2024. (Accessed 23 May 2025).
[16] B. Courter, V. Savane, J. Bi, S. Dev, C.J. Hansen, Finite element simulation of the fused deposition modelling process, in: NAFEMS World Congress, NAFEMS, 2017.
[17] Hexagon AB and/or its subsidiaries, Digimat-AM user guide, 2023, URL https://documentation-be.hexagon.com/bundle/Digimat_2023.3_AM_User_Guide/raw/resource/enus/Digimat_2023.3_AM_User_Guide.pdf, Version 2023.3. (Accessed 23 May 2025).
[18] X. Gao, S. Qi, X. Kuang, Y. Su, J. Li, D. Wang, Fused filament fabrication of polymer materials: A review of interlayer bond, Addit. Manuf. 37 (2) (2021) 101658, http://dx.doi.org/10.1016/j.addma.2020.101658.
[19] N.G. Tanikella, B. Wittbrodt, J.M. Pearce, Tensile strength of commercial polymer materials for fused filament fabrication 3D printing, Addit. Manuf. 15 (2017) 40–47, http://dx.doi.org/10.1016/j.addma.2017.03.005.
[20] O.S. Es-Said, J. Foyos, R. Noorani, M. Mendelson, R. Marloth, B.A. Pregger, Effect of layer orientation on mechanical properties of rapid prototyped samples, Mater. Manuf. Process. 15 (1) (2000) 107–122, http://dx.doi.org/10.1080/10426910008912976.
[21] Y. Zhou, H. Lu, G. Wang, J. Wang, W. Li, Voxelization modelling based finite element simulation and process parameter optimization for Fused Filament Fabrication, Mater. Des. 187 (2020) 108409, http://dx.doi.org/10.1016/j.matdes.2019.108409.
[22] A. Cattenone, S. Morganti, G. Alaimo, F. Auricchio, Finite element analysis of additive manufacturing based on fused deposition modeling: Distortions prediction and comparison with experimental data, J. Manuf. Sci. Eng. Trans. ASME 141 (2019) 1–17, http://dx.doi.org/10.1115/1.4041626.
[23] B. Brenken, A. Favaloro, E. Barocio, V. Kunc, R.B. Pipes, Thermoviscoelasticity in extrusion deposition additive manufacturing process simulations, in: American Society for Composites 2017, DEStech Publications, Inc., Lancaster, PA, 2017, pp. 705–720, http://dx.doi.org/10.12783/asc2017/15223.
[24] A. Trofimov, J. Le Pavic, S. Pautard, D. Therriault, M. Lévesque, Experimentally validated modeling of the temperature distribution and the distortion during the Fused Filament Fabrication process, Addit. Manuf. 54 (2022) 102693, http://dx.doi.org/10.1016/j.addma.2022.102693.
[25] P. Kulkarni, D. Dutta, Deposition strategies and resulting part stiffnesses in fused deposition modeling, J. Manuf. Sci. Eng. 121 (1) (1999) 93–103, http://dx.doi.org/10.1115/1.2830582.
[26] L. Li, Q. Sun, C. Bellehumeur, P. Gu, Composite modeling and analysis for fabrication of FDM prototypes with locally controlled properties, J. Manuf. Process. 4 (2) (2002) 129–141, http://dx.doi.org/10.1016/S1526-6125(02)70139-4.
[27] C. Casavola, A. Cazzato, V. Moramarco, C. Pappalettere, Orthotropic mechanical properties of fused deposition modelling parts described by classical laminate theory, Mater. Des. 90 (2016) 453–458, http://dx.doi.org/10.1016/j.matdes.2015.11.009.
[28] C. Ziemian, R. Ziemian, K. Haile, Characterization of stiffness degradation caused by fatigue damage of additive manufactured parts, Mater. Des. 109 (2016) 209–218, http://dx.doi.org/10.1016/j.matdes.2016.07.080.
[29] L. Sánchez-Balanzar, F. Velázquez-Villegas, L. Ruiz-Huerta, A. Caballero-Ruiz, A multiscale analysis approach to predict mechanical properties in fused deposition modeling parts, Int. J. Adv. Manuf. Technol. 115 (7) (2021) 2269–2279, http://dx.doi.org/10.1007/s00170-021-07287-w.
[30] S. Sharafi, M. Santare, J. Gerdes, S. Advani, A multiscale modeling approach of the fused filament fabrication process to predict the mechanical response of 3D printed parts, Addit. Manuf. 51 (2022) 102597, http://dx.doi.org/10.1016/j.addma.2022.102597.
[31] M. Lei, Y. Wang, Q. Wei, M. Li, J. Zhang, Y. Wang, Micromechanical modeling and numerical homogenization calculation of effective stiffness of 3D printing PLA/CF composites, J. Manuf. Process. 102 (2023) 37–49, http://dx.doi.org/10.1016/j.jmapro.2023.07.027.
[32] A. Nasirov, S. Hasanov, I. Fidan, Prediction of mechanical properties of fused deposition modeling made parts using multiscale modeling and classical laminate theory, in: Solid Freeform Fabrication 2019: Proceedings of the 30th Annual International Solid Freeform Fabrication Symposium – An Additive Manufacturing Conference, 2019.
[33] X. Liu, V. Shapiro, Homogenization of material properties in additively manufactured structures, Comput.-Aided Des. 78 (2016) 71–82, http://dx.doi.org/10.1016/j.cad.2016.05.017.
[34] K.-i. Kanatani, Distribution of directional data and fabric tensors, Internat. J. Engrg. Sci. 22 (2) (1984) 149–164.
[35] S.G. Advani, C.L. Tucker, The use of tensors to describe and predict fiber orientation in short fiber composites, J. Rheol. 31 (8) (1987) 751–784, http://dx.doi.org/10.1122/1.549945.
[36] M.E. Di Nardo, F. Frölich, L. Kärger, P. Carlone, Modeling time-dependent anisotropy in MEX component-scale process simulation, in: Materials Research Proceedings, Vol. 41, 2024, pp. 603–612, http://dx.doi.org/10.21741/9781644903131-67.
[37] J.K. Bauer, T. Böhlke, On the dependence of orientation averaging mean field homogenization on planar fourth-order fiber orientation tensors, Mech. Mater. 170 (2022) 104307, http://dx.doi.org/10.1016/j.mechmat.2022.104307.
[38] C. Krauß, J.K. Bauer, J. Mitsch, T. Böhlke, L. Kärger, On the averaging and closure of fiber orientation tensors in virtual process chains, J. Elasticity 156 (1) (2024) 279–306, http://dx.doi.org/10.1007/s10659-024-10050-3.
[39] J. Knirsch, F. Frölich, L. Hof, F. Wittemann, L. Kärger, pyGCodeDecode: A Python package for time-accurate GCode simulation in material extrusion processes, J. Open Source Softw. 9 (99) (2024) 6465, http://dx.doi.org/10.21105/joss.06465.
[40] J. Knirsch, F. Frölich, L. Hof, F. Wittemann, L. Kärger, pyGCodeDecode (1.3.1), 2025, http://dx.doi.org/10.5281/zenodo.14645536.
[41] T. Schultz, G. Kindlmann, A maximum enhancing higher-order tensor glyph, Comput. Graph. Forum 29 (3) (2010) 1143–1152, http://dx.doi.org/10.1111/j.1467-8659.2009.01675.x.
[42] F. A.M., Technical Data Sheet Ultrafuse PLA, Tech. rep., Forward AM, 2024, pp. 1–3, (Accessed 30 November 2024).
[43] F. Frölich, L. Hof, C. Zimmerling, F. Wittemann, L. Kärger, A submodeling approach for efficient prediction of local temperature profiles in component-scale additive manufacturing, Int. J. Adv. Manuf. Technol. 136 (2025) 1561–1576, http://dx.doi.org/10.1007/s00170-024-14913-w.
[44] A. Elkholy, M. Rouby, R. Kempers, Characterization of the anisotropic thermal conductivity of additively manufactured components by fused filament fabrication, Prog. Addit. Manuf. 4 (2019) 497–515, http://dx.doi.org/10.1007/s40964-019-00098-2.
[45] J.A. Tröger, C. Steinweller, S. Hartmann, Identification, uncertainty quantification and validation of orthotropic material properties for additively manufactured polymers, Mech. Mater. 197 (2024) 105100, http://dx.doi.org/10.1016/j.mechmat.2024.105100.
[46] F. Frölich, L. Bechtloff, B.M. Scheuring, A.L. Heuer, F. Wittemann, L. Kärger, W.V. Liebig, Evaluation of mechanical properties characterization of additively manufactured components, Prog. Addit. Manuf. 10 (2025) 1217–1229, http://dx.doi.org/10.1007/s40964-024-00700-2.
[47] F. Frölich, D. Dörr, A. Jackstadt, F. Wittemann, L. Kärger, Mechanical and kinetic characterization of additively manufactured PLA structures for improved process and warpage modeling, Mater. Res. Proc. 54 (2025) 2281–2290, http://dx.doi.org/10.21741/9781644903599-246.
[48] J.M. Svanberg, J.A. Holmberg, Prediction of shape distortions Part I. FE-implementation of a path dependent constitutive model, Compos. A 35 (6) (2004) 711–721, http://dx.doi.org/10.1016/j.compositesa.2004.02.005.
[49] B. Brenken, Extrusion Deposition Additive Manufacturing of Fiber Reinforced Semi-Crystalline Polymers (Ph.D. thesis), Purdue University, School of Aeronautics & Astronautics, 2017.